

Article

Petrogenesis and Tectonic Setting of the Baluogenguole Mafic Dykes, Zongwulong Belt: Implications for Evolution of the Northern East Paleo-Tethys Ocean

Min Chen ¹, Tong Pan ², Wen-Tao Zhao ¹, Yan-He Wang ^{3,*}, Chun-Ji Xue ⁴, Bing-Zhang Wang ² and Chu-Lin Xia ¹

¹ School of Geological Engineering, Qinghai University, Xining 810016, China; chenmin_cn@163.com (M.C.); zhaowen168@163.com (W.-T.Z.); xiachulin@163.com (C.-L.X.)

² Bureau of Geological Exploration and Development of Qinghai Province, Xining 810008, China; pant66@163.com (T.P.); wbz6901@126.com (B.-Z.W.)

³ Xining Natural Resources Investigation Center, China Geological Survey, Xining 810000, China

⁴ School of Earth Science and Resources, China University of Geosciences, Beijing 100190, China; chunji.xue@cugb.edu.cn

* Correspondence: wyhxnzx@163.com

Abstract: The late Paleozoic tectonic setting of the Zongwulong Belt (ZWL B), a significant unit located in the northern Qaidam margin, Qinghai province, remains uncertain. Diabase dykes in the western part of the Zongwulong Belt offer insights into this issue. Field investigations reveal that the dips of the dykes are almost vertical, and they have sharp boundaries with the host rocks. These dykes consist of plagioclase, clinopyroxene, and opaque minerals exhibiting a characteristic porphyritic texture and massive structure. Zircon U-Pb dating of the dykes yields a weighted ²⁰⁶Pb/²³⁸U age of 289 ± 1 Ma. The dykes exhibit relatively high concentrations of TFeO, K₂O + Na₂O, and TiO₂, while the SiO₂ and MgO concentrations are relatively low. They display relative light-over-heavy REE enrichment, and lack negative Nb-Ta and Eu anomalies. The dykes underwent negligible crustal contamination, and experienced extensive fractional crystallization of olivine, clinopyroxene, and Fe-Ti oxides. Originating from the spinel-garnet transition zone at depths of approximately 75 km, the dykes result from garnet facies low-degree melting (5%–10%) in a continental rift setting. Combining these findings with regional geological data, we propose that the ZWL B likely experienced a continental rift in the west and exhibited a narrow oceanic environment in the east in the late Paleozoic period, potentially representing the most distant north branch of the East Paleo-Tethys Ocean.

Keywords: Baluogenguole mafic dykes; geochemistry; late Paleozoic; East Paleo-Tethys Ocean; Zongwulong Belt



Citation: Chen, M.; Pan, T.; Zhao, W.-T.; Wang, Y.-H.; Xue, C.-J.; Wang, B.-Z.; Xia, C.-L. Petrogenesis and Tectonic Setting of the Baluogenguole Mafic Dykes, Zongwulong Belt: Implications for Evolution of the Northern East Paleo-Tethys Ocean.

Minerals **2024**, *14*, 473. <https://doi.org/10.3390/min14050473>

Received: 20 March 2024

Revised: 20 April 2024

Accepted: 25 April 2024

Published: 29 April 2024



Copyright: © 2024 by the authors. Licensee MDPI, Basel, Switzerland. This article is an open access article distributed under the terms and conditions of the Creative Commons Attribution (CC BY) license (<https://creativecommons.org/licenses/by/4.0/>).

1. Introduction

The NW-trending Zongwulong Belt (hereinafter referred to as ZWL B) is sandwiched between the Qilian Orogen and the northern margin of the Qaidam Basin, with its eastern extension reaching into the junction of the East Kunlun and West Qinling orogens (Figure 1b, [1]). The main strata of the ZWL B are characterized by late Paleozoic to early Mesozoic sedimentary rocks, including the Tianjunnanshan Carboniferous ophiolite complex [2]. This ophiolite complex is coeval with those at Muztagh–Buqingshan–Anemaqen (303–345 Ma, [3,4]) and the Kuhai–Saishitang (369 ± 1 Ma, [5]) district, representing one of the main parts of the Paleo-Tethys Ocean suture zone. Therefore, the ZWL B could serve as a key window for deciphering the formation of Paleo-Tethys Ocean in the northernmost Qinghai–Tibet Plateau.

The ZWL B was initially considered a late Paleozoic continental rift ([6,7]). Since the discovery of the Carboniferous Tianjunnanshan ophiolite by Wang [2], this belt was first regarded as having formed in an oceanic setting. In contrast, Fu [8] identified 509 ± 4 Ma

dolerite in the Tianjunnanshan ophiolite and proposed that the ZWLB is an early Paleozoic to early Mesozoic composite orogen formed after the closure of the Proto- to Paleo-Tethys oceans. However, the Wahongshan–Wenquan (WWF) strike-slip fault has cut the ZWLB into western and eastern parts, and the rocks in both parts are completely different. In its eastern part, there are ophiolites representing oceanic crust fragments [2,8] and late Paleozoic to early Mesozoic granitoids related to oceanic subduction and continental collision [9–14]. Conversely, there are no comparable ophiolites and their rock fragments and arc-type granitoids have been found in the western ZWLB.

Recently, a number of Li–(Be) rare-metal pegmatite veins have been discovered in the Chakabeishan area in eastern ZWLB [15,16], forming a potential Li-bearing ore belt. The ambiguous tectonic affinities of the ZWLB have hampered future exploration, particularly regarding the Li-Be mineralization potential.

Mafic dykes exhibit a fast emplacement rate and experience a low degree of crustal contamination, which may largely retain the nature of the mantle source and can provide insights into deep processes [17,18]. We have discovered a series of Early Permian mafic dykes in the Baluogenguole area in the western ZWLB. Field geological surveys, petrographic and geochemical analysis, as well as zircon U-Pb dating and Sr-Nd-Hf isotope analysis, were carried out to explore their petrogenesis and tectonic setting. The implications of this study for the regional tectonic evolution will also be discussed.

2. Geological Setting

The Central China Orogenic Belt (hereinafter referred to as CCOB) is a 5000 km long tectonic belt stretching from east to west across Central China. The Qilian–Qaidam–Kunlun (QQK) orogen in the northern Tibetan Plateau constitutes the western part of the CCOB (Figure 1a, [19,20]). The QQK orogen is considered to have formed through a complex accretion–collision sequence involving the Proto- to Paleo-Tethyan Oceans from the Paleozoic to early Mesozoic (e.g., [8,21–28]).

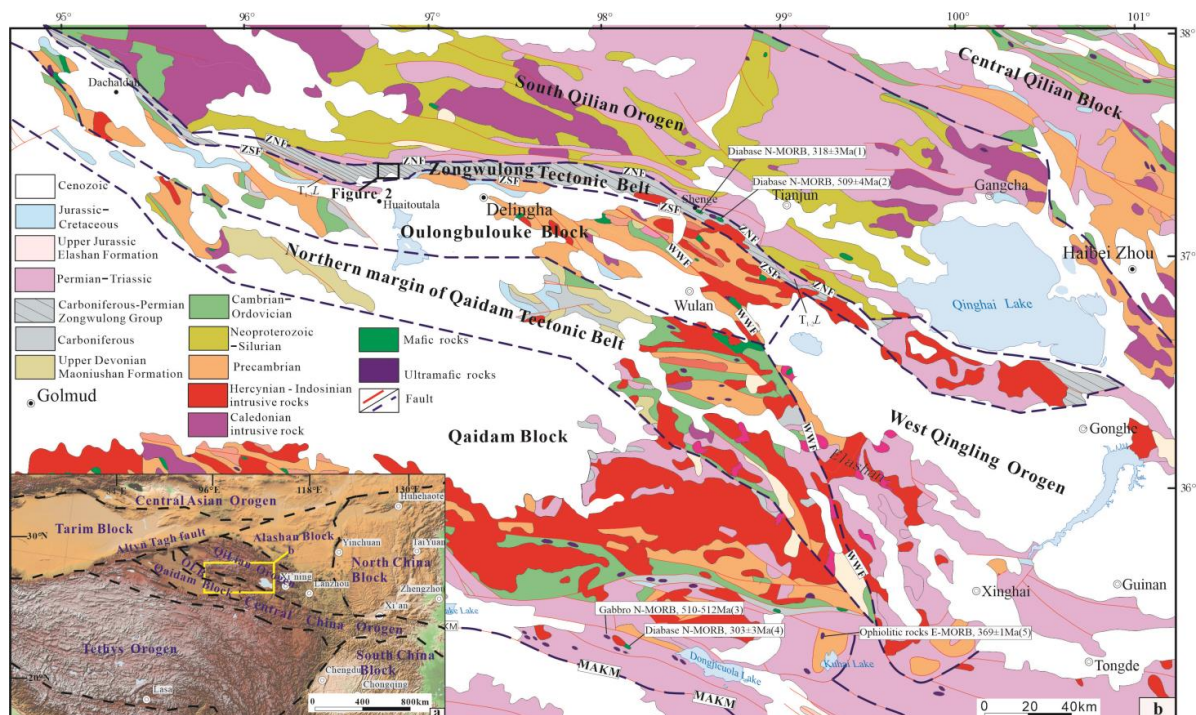


Figure 1. Tectonic framework of the western part of CCOB ((a), modified after Yang [22]) and geological map of the ZWLB and adjacent areas ((b), modified after Pan [29]); MAKM—Muztagh–Buqingshan–Anemaqen; WWF—Wahongshan–Wenquan Fault; ZSF—Zongwulong Southern Margin Fault; ZNF—Zongwulong Northern Margin Fault.

The ZWLB has a length of about 500 km and a width of 5 to 10 km. It is bounded by the South Qilian Belt, with the Zongwulong Northern Margin Fault to the north, and by the Oulongbulouke Block, with the Zongwulong Southern Margin Fault to the south. Additionally, it is cut to the west by the Altyn Tagh Fault during the Mesozoic [30], and it may extend eastward to the West Qinling Orogen (Figure 1b, [6,8,9,12,25,31]).

The Oulongbulouke Block is considered to represent a basement fragment derived from the Tarim Craton [26,32]. It has a typical two-layer structure with a Paleo- to Mesoproterozoic metamorphic basement and a Neoproterozoic sedimentary cover [33–36]. Overlying the Precambrian strata are lower Paleozoic carbonate sediments that underwent the Caledonian orogeny and Silurian arc–continent collision [37]. The upper Paleozoic sequence comprises Middle–Late Devonian terrestrial clastic–volcanic rocks, and widespread Carboniferous–Permian marine and continental interclastic sediments with carbonate interlayers. The Devonian Maoniushan Formation mainly consists of an upper bimodal volcanic rock sequence (ca. 411–409 Ma) and the lower clastic rocks [38]. Tuff has recently been identified in the Carboniferous–Permian sediments (Zhabusagaxiu Formation), with a high-precision age determined to be 293–295 Ma [39,40].

The South Qilian Belt is considered to display affinity with the South China Block [23,41,42], and is mainly represented by a Mesoproterozoic crystalline basement, lower Paleozoic fold basement, and upper Paleozoic to early Mesozoic sedimentary cover (Figure 1b). In response to the subduction and closure of the Proto-Tethyan Ocean, the South Qilian Belt formed a large number of early Paleozoic intermediate–acid magmatic rocks, with its western segment unconformably overlain by the Silurian and Triassic sedimentary rocks [23,42,43].

The ZWLB differs from the petrostratigraphic units developed in the Precambrian blocks on the north and south sides. It is embedded in the CCOB, representing a Proto- to Paleo-Tethyan tectonic domain. The ZWLB is primarily represented by the Carboniferous–Permian Zongwulong Group (including the Turgendaban and Guokeshan Formations), the Triassic Longwuhe Formation, and Carboniferous Tianjunnanshan ophiolitic rocks, which are associated with the evolution of the Paleo-Tethys Ocean [1,8,9]. With the Wahongshan Fault serving as the boundary (Figure 1b), significant differences are observed between the eastern and western parts of the ZWLB. In the western ZWLB, the Zongwulong Group primarily consists of the Turgendaban Formation, intruded by mafic dykes. The Turgendaban Formation exhibits flysch sedimentary characteristics, consisting of semi-abyssal to abyssal facies feldspar quartz sandstone, lithic quartz sandstone with limestone and mudstone, and some volcanic rocks. The Longwuhe Formation is restricted to the Huaitoutala area; its rocks consist of sandstone, slate with laminated limestone, and conglomerate with sandstone appearing upward, displaying molasse unit features [44,45]. Late Paleozoic to early Mesozoic arc-type granitoids and ophiolites, or their rock fragments, are absent in the western ZWLB. In the eastern ZWLB, the Zongwulong Group comprises the Turgendaban and Guokushan Formations, which are in fault contact. The Guokeshan Formation is composed of shallow-marine lithic quartz sandstone interbedded with limestone [2,7–9]. The Longwuhe Formation is widely distributed and shares similarities with the Longwuhe Formation of the West Qinling Orogen, displaying typical flysch clastic rock deposition [46]. Ophiolites in the Tianjunnanshan area, comprising ultramafic rocks, gabbro, dolerite, basalt, and chert [2,8], indicate the presence of the Proto-Tethys and Paleo-Tethys oceanic crusts [8,9]. Additionally, late Paleozoic to early Mesozoic granitoids related to oceanic subduction and continental collision have also developed in the eastern ZWLB [9–14].

3. Geology and Sample Descriptions of Baluogenguole Mafic Dykes

The studied mafic dykes are located in the western ZWLB, approximately 25 km northeast from the town Huaitoutala (Figure 1b). These dykes have intruded phyllites and exhibit a thickness ranging from 0.5 m to 3 m, with a maximum length up to 5 km (Figures 2 and 3a). They strike east–west (EW) and are nearly vertical (Figures 2 and 3b). The contact boundary between the mafic dykes and the host rocks is sharp (Figure 3c).

Strong cleavage zones, approximately 20 cm to 100 cm wide, are observed at the edge of the host rocks (Figure 3c). The host rocks mainly consist of phyllite of the Zongwulong Group and also strike east–west, consistent with the trend of the dykes (Figure 2).

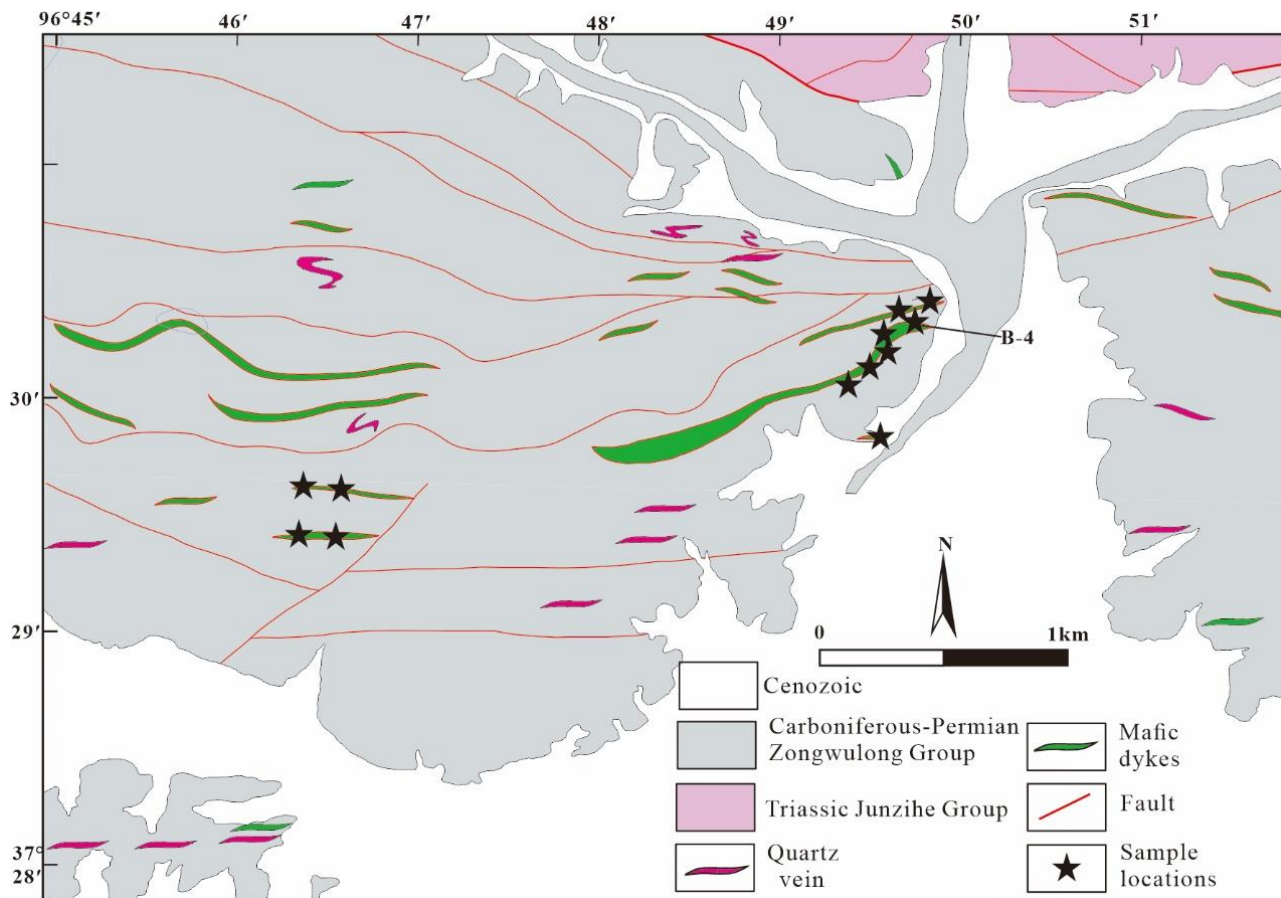


Figure 2. Simplified geological map of the Baluogenguole mafic dykes.

A total of 12 unaltered dyke samples (1-1, 2-1, 3-2, 4-1, 4-2, 5-1, 5-2, 6-2, 7-1, 7-2, 8-1, and 8-2) were collected from different locations (Figure 2). Among these, sample 4-1 (B-4), collected from mafic dyke No.3, was selected for U-Pb dating (Figure 2). The mafic dykes mainly comprise diabase porphyrite, and are grey-green in color with an ophitic texture and a massive structure. They are composed of phenocrysts (10%) and groundmass (90%). The phenocrysts consist of plagioclase (8%) and dark-colored minerals (2%). Plagioclase phenocrysts are tabular and exhibit strong alterations, including those from carbonate, chlorite, and epidote. While the altered plagioclase type is not easy to measure, we can only speculate it to have originally been calcic feldspar. The dark-colored minerals are short, columnar, and granular, and they are replaced by carbonate minerals, chlorite, and aggregates of epidote. These minerals are believed to have mainly been clinopyroxene based on their crystal morphology. The groundmass exhibits an ophitic texture and is mainly composed of plagioclase (46%), dark-colored clinopyroxene and biotite (38%), opaque titanomagnetite (6%), and very few quartz. Both the plagioclase and dark-colored minerals show strong alteration (Figure 3d,e).

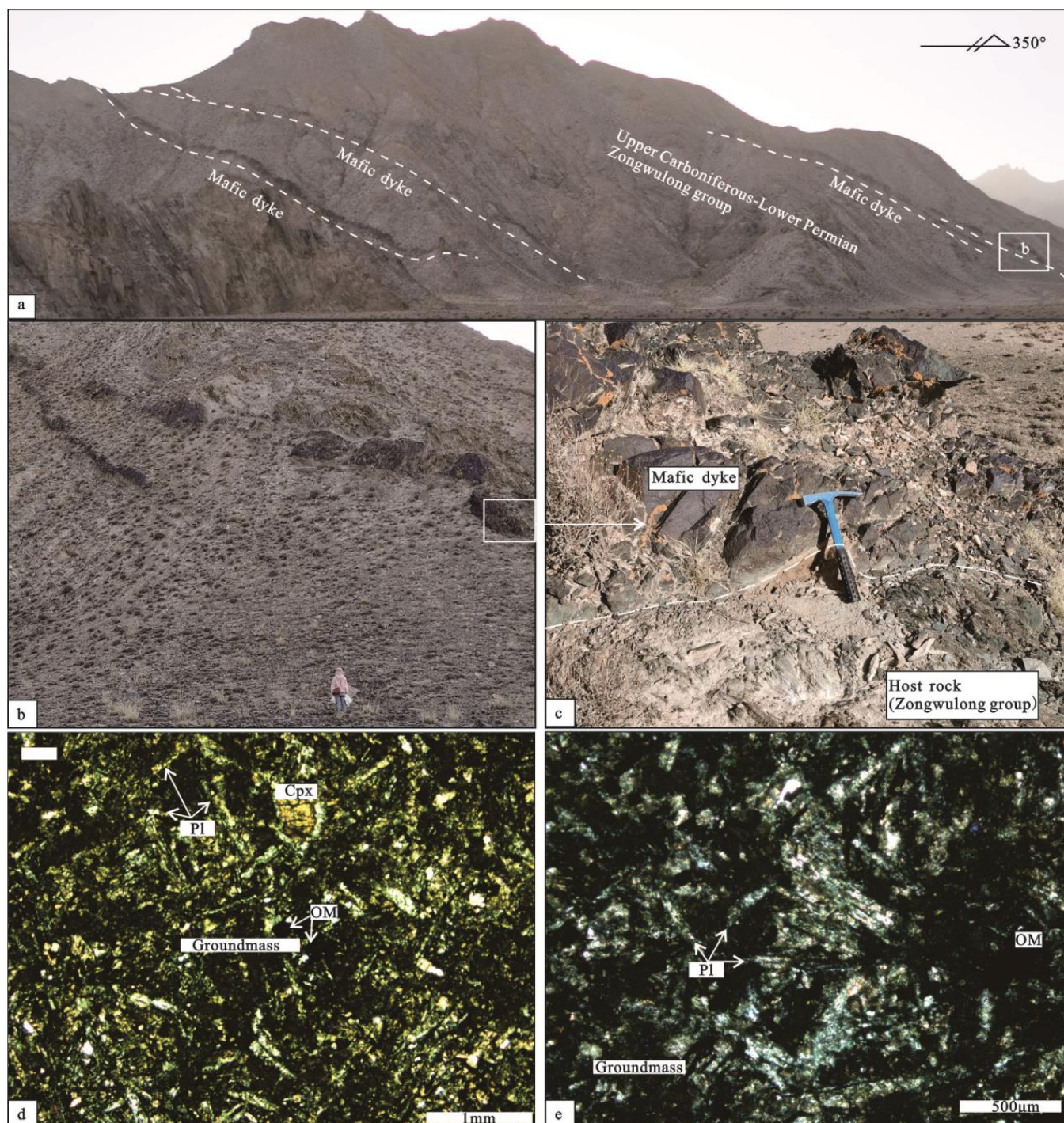


Figure 3. Outcrop of the NW-striking Baluogenguole mafic dykes intruding the Zongwulong Group (a,b); outcrop of host rocks (Zongwulong Group) with strong cleavage zones (c); and photomicrograph of the Baluogenguole diabase dykes, composed of phenocrysts (Pl + Cpx) and groundmass (Pl + Cpx + OM) ((d,e), cross-polarized light). Abbreviations: Cpx—clinopyroxene, Pl—plagioclase, OM—opaque titanomagnetite.

4. Analytical Methods

4.1. Whole-Rock Geochemical Analysis

All samples were cleaned, with any weathered or veined surfaces were removed using a diamond saw. This was followed by washing with distilled water and air-drying. The samples were then crushed and pulverized to 200 mesh. Whole-rock major and trace

element abundances were analyzed using a PANalytical Axios-advance X-ray fluorescence spectrometer (XRF) and Elan DRC-e ICP-MS, respectively, at Nanjing Hongchuang Geological Exploration Technology Service Co., Ltd. (NHEXTS), Nanjing, China. The analytical precision of the whole-rock major elements is better than $\pm 5\%$. The analytical precision of the whole-rock trace elements matches that reported by Liu [47]. The detailed procedure followed the methodology described by Chen [13].

4.2. Zircon U-Pb Dating

In total, more than 300 zircon grains from a 25 kg diabase dyke sample (B-4) were extracted using standard heavy liquid and magnetic techniques. Idiomorphic zircon grains were handpicked under a binocular microscope and then mounted in epoxy along with the zircon standard R33 [48]; the surface of the grains was then polished to expose the center of the grains. Afterwards, reflected-light photomicrographs were taken and cathodoluminescence (CL) imaging was conducted, followed by LA-ICP-MS analysis at NHEXTS. The internal structure of zircon grains was analyzed employing a TESCAN MIRA3 field emission scanning electron microscope and TESCAN cathode luminescence probe. The selection of test points was firstly based on the reflected light and transmitted light micrographs of zircons, and then compared repeatedly with CL images to identify and avoid internal cracks and inclusions, in order to obtain more accurate age information. In situ U-Pb dating and trace element analysis of zircons were conducted using an LA-ICP-MS instrument equipped with an Agilent 7700 \times quadrupole mass spectrometer and a Photon Machines Excite laser ablation system. The laser employed is a 193 nm ArF excimer laser. The direct laser ablation beam diameter is 35 μm , and the sample ablation depth ranges from 20 to 40 μm . Zircon 91500 and GJ-1 were used as primary and secondary reference materials, respectively [49]. Triplets of 91500 and GJ-1 were bracketed between multiple groups of 10 to 12 sample unknowns. Typically, 35–40 s of the sample signals were acquired after 20 s gas background measurement. Using the exponential function to calibrate the downhole fractionation [50]. NIST 610 and ^{91}Zr were used to calibrate the trace element concentrations as the external reference material and internal standard element, respectively. Measured ages of 91500 (1061.5 ± 3.2 Ma, 2σ) and GJ-1 (601.7 ± 4.2 Ma, 2σ) are well within 1% of the accepted age. The ICPMS-DataCal and Isoplot/Exver (Version3.0) software were used for data reduction [51,52]. Trace element contents were calibrated using NIST SRM 610, a synthetic silicate glass made by the National Bureau of Standards and Technology, as the external standard, and Si as an internal standard. The analytical procedures followed were consistent with those described by Liu [52].

4.3. Zircon Lu-Hf Isotopes

Zircon Lu-Hf isotope analyses were also measured at NHEXTS. In situ Hf isotope ratio analyses of zircon were conducted on the dated zircon grains. This was achieved using an Australian Scientific Instruments *RESOLUTION LR* laser ablation system (Canberra, Australian) and Nu Instruments MC-ICP-MS (Wrexham, Wales, UK). The 193 nm ArF excimer laser, which was homogenized by a set of beam delivery systems, was focused on the zircon surface with a fluence of 3.5 J/cm². The ablation protocol employed a spot diameter of 50 μm at an 8 Hz repetition rate for 40 s, which equates to 320 pulses. Helium was applied as carrier gas to efficiently transport aerosol to the MC-ICP-MS. Standard zircons (including GJ-1, 91500, Plešovice, Mud Tank, Penglai) were treated as quality control every five unknown samples. Zircon Plešovice was used as the reference standard. The average value of the standard's $^{176}\text{Hf}/^{177}\text{Hf}$ ratio was 0.282481 ± 0.000010 (2σ), which is in good agreement with the reference value of 0.282482 ± 0.000013 [53].

4.4. Whole-Rock Sr-Rb and Sm-Nd Isotope Analysis

The analysis of whole-rock Sr-Nd isotope composition of the mafic dyke samples was conducted at NHEXTS. Following the separation and purification of Sr-Rb and

Sm-Nd isotopes, the compositions of whole-rock powders for Sr-Rb and Sm-Nd isotopes were determined using the Neptune plus MC-ICP-MS (Thermo Fisher Scientific, Dreieich, Germany).

The mass fractionation of the $^{87}\text{Sr}/^{86}\text{Sr}$ ratio was corrected by normalization to a constant $^{86}\text{Sr}/^{88}\text{Sr}$ ratio of 0.1194, employing an exponential law. The isobaric interference of ^{87}Rb on ^{87}Sr was corrected using a natural $^{87}\text{Rb}/^{85}\text{Rb}$ ratio of 0.3857. Instrumental drift was corrected using the NIST SRM 987 standard as external reference [54,55].

The mass bias correction of the $^{143}\text{Nd}/^{144}\text{Nd}$ ratio was conducted by normalizing to $^{146}\text{Nd}/^{144}\text{Nd} = 0.7219$, employing an exponential fractionation law. Instrumental drift was corrected using the JNdi-1 standard as external reference [56].

5. Results

5.1. Whole-Rock Major and Trace Elements

The whole-rock major and trace element compositions of the twelve dyke samples are presented in Supplementary Table S1. The data for coeval mafic magmatism related to the Paleo-Tethys Ocean are provided for comparison, including ca. 318–331 Ma Tianjunnanshan mafic rocks (TJNS, [2,8]), ca. 317–279 Ma high-Ti continental mafic dykes in the south Qiangtang Block (QHT, [57–59]), ca. 303 Ma Buqingshan N-MORB mafic rocks (BQS) in the East Kunlun Orogen [4], and 359–387 Ma Lalongwa mafic dykes (LLW) in the Kuhai-Saishitang Tectonic Belt [1,5,60]. The loss on ignition (5.28–12.17 wt.%) of the samples is relatively high, suggesting that the mafic dykes have undergone alteration; this is consistent with the microscopic observations (Figure 3). All the major element concentrations in these samples are normalized to 100% on a volatile-free basis.

The mafic dykes exhibit relatively uniform SiO_2 (47.3–51.8 wt.%) and Na_2O (2.26–3.92 wt.%) contents, but the content of K_2O (0.08–1.10 wt.%) varies greatly. They also display relatively high TiO_2 (2.02–4.05 wt.%) and $\text{T}_{\text{Fe}_2\text{O}_3}$ (12.67–15.91 wt.%) contents, as well as low MgO (4.11–7.50 wt.%), variable Al_2O_3 (13.54–17.00 wt.%), and low P_2O_5 (0.24–0.51 wt.%) contents. The Mg\# ($=\text{MgO}/(\text{MgO} + \text{FeO} + \text{Fe}_2\text{O}_3)$, molar ratios) values of the samples range from 34.1 to 52.3, and are lower than the Mg\# value of the original basaltic magma (68–75, [61]). Most of the samples fall into the gabbroic field and around the boundary between subalkaline and alkaline rocks in a total alkalis versus SiO_2 diagram (Figure 4a, [62]). However, they exhibit high Nb/Y ratios (0.67–1.76), comparable to those of the QHT. In an immobile element diagram (Figure 4b), all of the samples fall into the alkaline basalt field (Figure 4b).

In contrast, the TJNS, BQS, and LLW samples belong to the Andesite or basalt field, close to the boundary to the subalkaline basalt field due to their low Nb/Y ratios (Figure 4a, [63]).

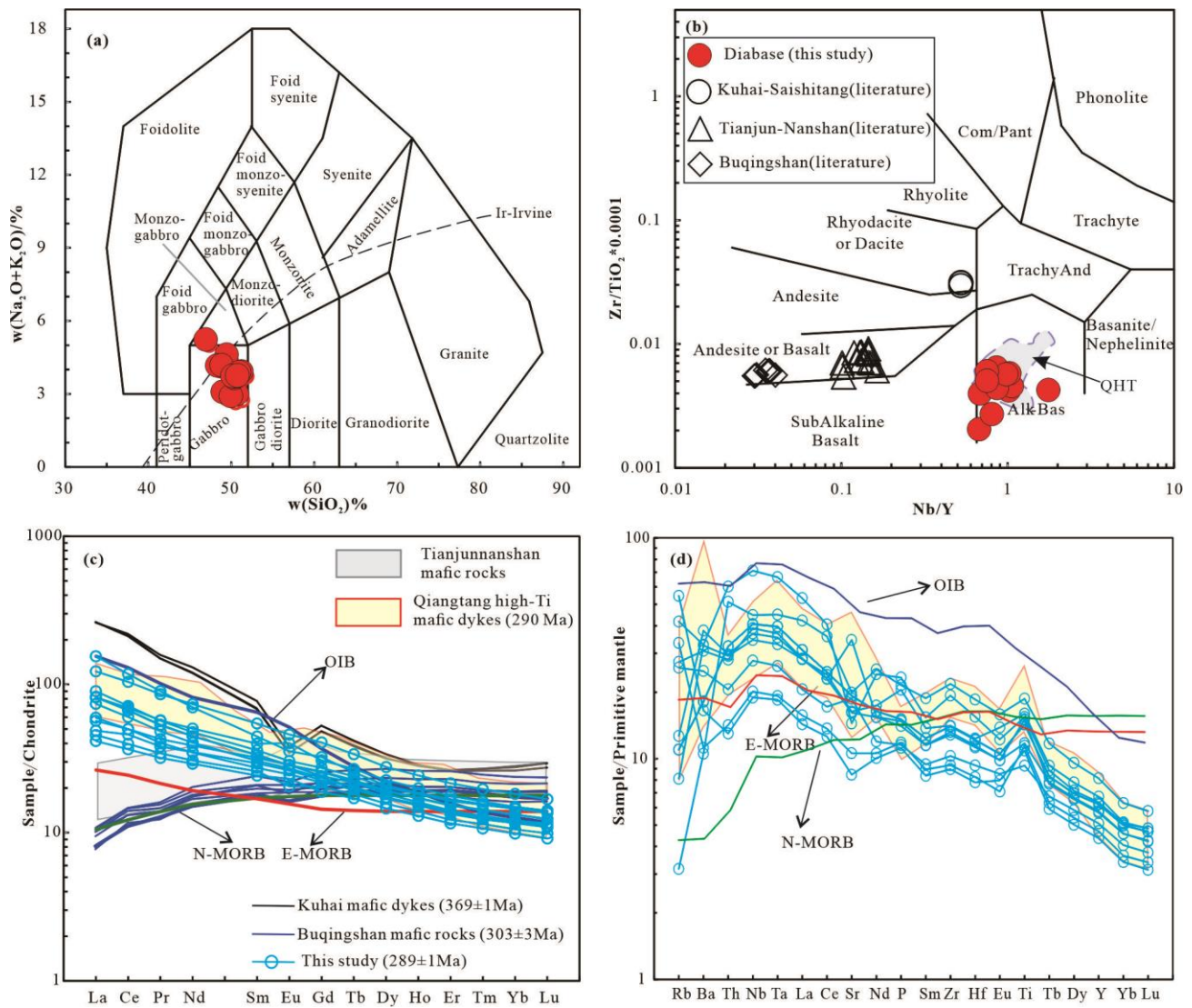


Figure 4. (a) $\text{Na}_2\text{O} + \text{K}_2\text{O}$ versus SiO_2 plot (after [62]); (b) Zr/TiO_2 versus Nb/Y plot (after [63]); (c) chondrite-normalized REE patterns; (d) primitive-mantle-normalized multi-element spidergram. Chondrite and primitive-mantle-normalized values are derived from [64]. Note: OIB, N-MORB, E-MORB data are sourced from [64]. Data for Tianjunnanshan mafic rocks, Kuhai–Saishitang mafic dykes, Buqingshan mafic rocks, and Qingtang high-Ti mafic dykes are from [1,4,8,9,57–59], respectively. The symbols and data sources in this figure are consistent with those in Figures 7 and 9–11.

The diabase samples exhibit varying V, Cr, and Ni contents ranging from 216.25 to 355.71 ppm, 32.27 to 312.40 ppm, and 31.48 to 153.04 ppm, respectively. They display uniform chondrite-normalized REE patterns, characterized by LREE-enriched patterns $[(\text{La}/\text{Yb})_{\text{N}} = 4.21\text{--}10.51]$ with negligible Eu anomalies ($\text{Eu}/\text{Eu}^* = 0.89\text{--}1.15$) (Figure 4c). These samples are enriched in High-Field-Strength Elements (HFSEs) such as Nb, Ta, and Ti, resembling OIB-like alkaline basalts [65,66] on the primitive-mantle-normalized spidergram (Figure 4d). Their REE and trace element patterns are similar to those of the QHT but differ from the TJNS, BQS, and LLW samples (Figure 4c,d).

5.2. Zircon U–Pb Geochronology

The zircon grains extracted from sample B-04 in the ZWLB underwent LA–MC–ICP–MS U–Pb dating. Representative CL images of the zircon grains from the diabase sample (B-4) are depicted in Figure 5a. The U–Pb isotope analytical results are provided in

Supplementary Table S2, while the weighted average ages and Concordia diagrams are presented in Figure 5b,c, respectively.

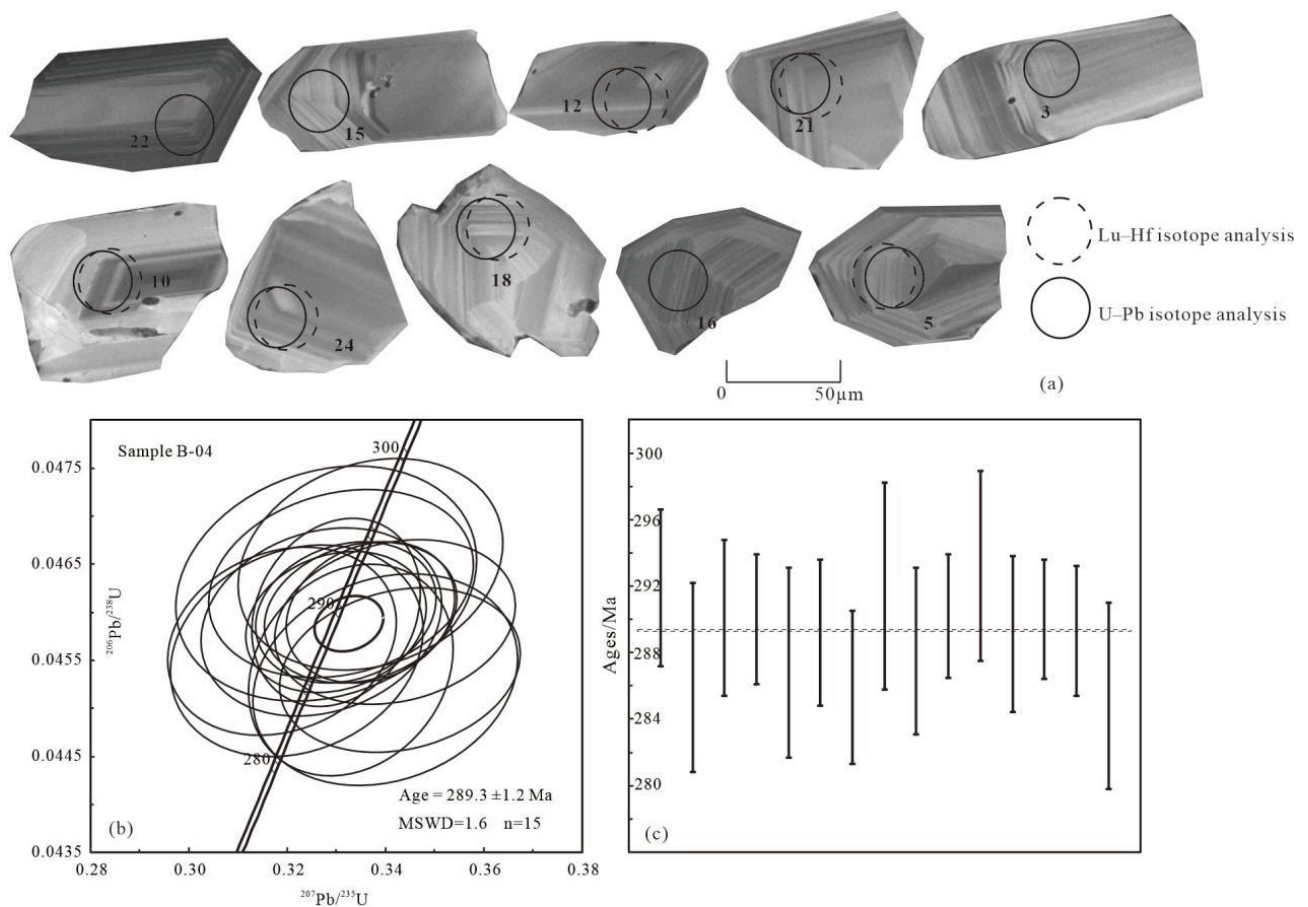


Figure 5. CL images of representative zircon grains from mafic dykes (a) and zircon U–Pb concordant diagram for sample B-04 (b,c) in the ZWLB.

Twenty-five zircon grains from diabase sample B-4 were analyzed. These zircons typically appear transparent, ranging from colorless to pale yellow, and exhibit euhedral or subhedral shapes. Their lengths vary between 40 and 110 μm , and the width/length ratios range, approximately, from 1.1 to 2.5. Notably, the zircon grains display distinct oscillatory zonings and high Th/U ratios (0.4 to 1.2), indicative of a magmatic origin [67–69]. Among the twenty-five analyzed spots, six data points show concordances of less than 95% (see Supplementary Table S2). Three zircon grains yielded significantly older $^{206}\text{Pb}/^{238}\text{U}$ ages (434–442 Ma), consistent with inherited zircons and arc-related volcano-sedimentary assemblages of the Tanjianshan Group and the High-Pressure–Ultra-High-Pressure (HP-UHP) metamorphic complexes in the North Qaidam Orogen [70,71]. The remaining fifteen analytical spots yielded concordant $^{206}\text{Pb}/^{238}\text{U}$ ages between 285 and 292 Ma (Supplementary Table S2), with a weighted mean of 289.3 ± 1.2 Ma (MSWD = 1.6) (Figure 5b,c). We interpret this as the crystallization age of the sample.

5.3. Sr–Nd–Hf Isotope Compositions

Whole-rock Rb–Sr and Sm–Nd data for Baluogenguole mafic dykes are presented in Supplementary Table S3. The initial Sr–Nd isotope values were calculated using the weighted mean age of 289.3 Ma for sample B-04. The samples exhibit variable $(^{87}\text{Sr}/^{86}\text{Sr})_i$ values ranging from 0.71587 to 0.72251, relatively uniform $(^{143}\text{Nd}/^{144}\text{Nd})_i$ values ranging from 0.512525 to 0.512687, and $\epsilon\text{Nd}(t)$ values ranging from +5.07 to +8.23, respectively.

They have yielded corresponding single-stage Nd model ages (T_{DM}) ranging from 333 to 449 Ma.

Supplementary Table S4 contains the in situ zircon Hf isotope data for the No.3 mafic dyke sample B-4. The zircon grains exhibit positive $\epsilon_{Hf}(t)$ values ranging from +1.31 to +3.58 and relatively young single-stage Hf model ages ranging from 783 to 862 Ma.

6. Discussion

6.1. Post-Magmatic Alteration

Although the freshest rocks were selected for chemical analysis, the LOI values (5.28–12.17 wt.%) are still high, indicating significant post-magmatic alteration in the mafic dykes. This is consistent with observations from the microscopic mineralogy that the plagioclase and clinopyroxene show strong alteration. This highlights the necessity of assessing the intensity of alteration effects on the whole-rock geochemical data.

The alteration in plagioclase results in the high mobility of major elements (e.g., Na_2O , K_2O , Al_2O_3 , CaO), while the alteration in clinopyroxene leads to the high mobility of major elements such as MgO and TFeO. However, since the content of clinopyroxene in the sample rocks is low (2%), the influence of clinopyroxene alteration on MgO and TFeO is limited (Figure 6a,b).

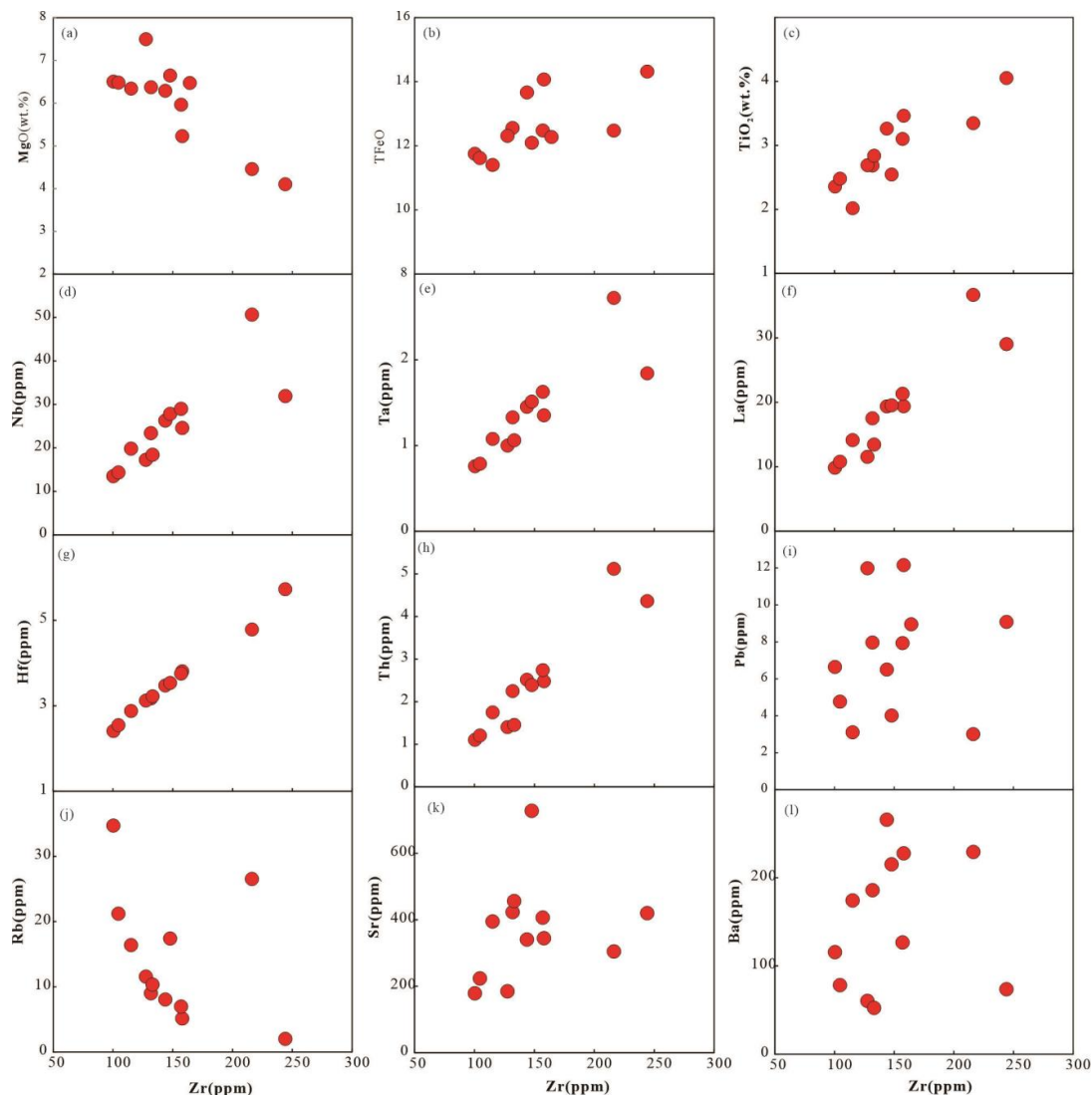


Figure 6. (a–l) Plots of MgO, TFeO, TiO_2 , Nb, Ta, La, Hf, Th, Pb, Rb, Sr, and Ba vs. Zr for the Baluogenguole diabase samples.

Zr in igneous rocks is commonly considered one of the most immobile elements during low- to medium-grade metamorphism and alteration, except for the case of intense seafloor hydrothermal alteration (e.g., [72,73]). The influence of post-magmatic alteration on other trace elements can be assessed based on correlations with the Zr content [74]. As shown in Figure 6, the positive correlations between HFSEs and Zr suggest that these elements have retained their original signatures. However, there are no correlations between the contents of Ba, Rb, Pb, and Sr (LILE) and the Zr content, indicating the high mobility of these elements during alteration. Post-magmatic alteration may also influence the Sr isotopic composition, potentially providing misleading information about the mantle source [75].

To minimize the effects of alteration, major elements such as MgO, TFeO, and TiO₂, as well as trace elements including highly incompatible elements (HFSEs), Th, and rare earth elements (REEs), were used to constrain the petrogenesis and tectonic setting of the mafic dykes.

6.2. Petrogenesis and Magma Sources

6.2.1. Crustal Contamination

Mafic dykes intruded into continental environments can experience contamination from the surrounding continental crust either during their ascent or while residing within the crust. The presence of inherited zircons, enriched in light REEs, and depleted in heavy REEs, suggest that limited crustal contamination might have occurred during the ascent of the mafic magma. In the primitive-mantle-normalized trace element spidergram, the average continental crustal compositions show an obvious depletion in Nb–Ta [76], which is distinct from the pattern of the studied Baluogenguole mafic rocks (Figure 4d), precluding the possibility of widespread continental contamination. Both Th and Ta are also sensitive to crustal contamination. The primitive mantle has a Th/Ta ratio of 2.3, while the typical upper continental crust has a Th/Ta ratio greater than 10 [77]. The samples have a mean Th/Ta value of 1.72, which also indicates that continental contamination is negligible.

The samples have substantially lower La/Nb ratios (0.67 to 0.91) than typical continental crustal rocks (>12), along with a restricted range of zircon $\epsilon\text{Hf}(t)$ and whole-rock $\epsilon\text{Nd}(t)$ values, which is inconsistent with continental contamination. Additionally, no/weak negative and positive correlations are observed for SiO₂ (wt.%) vs. Th/Nb, SiO₂ (wt.%) vs. La/Sm, and Nb/La vs. Sm/Nd, respectively (Figure 7a–c), suggesting a negligible contribution from ancient continental crust. In the Th/Yb vs. Nb/Yb diagram (Figure 8a), the samples do not exhibit a conspicuous shift toward high Th/Yb ratios and deviation from the mantle array, indicating that the dyke magmas retained the features of their mantle source. A $(\text{La}/\text{Nb})_{\text{PM}}$ vs. $(\text{Th}/\text{Nb})_{\text{PM}}$ diagram also indicates the lack of continental crust input (Figure 7d, [78]). The samples are plotted within the field defined by Hawaiian OIB-like alkaline basalts [79] and least-contaminated Qiangtang high-Ti alkaline mafic rocks [57–59], suggesting the dyke magmas retained the features of their mantle source.

Furthermore, Baluogenguole mafic dykes exhibit a distinct intrusive relationship with the host rocks in the field, indicating that the crustal contamination is insignificant. Thus, the observed geochemical diversity most likely reflects the nature of the mantle source [80].

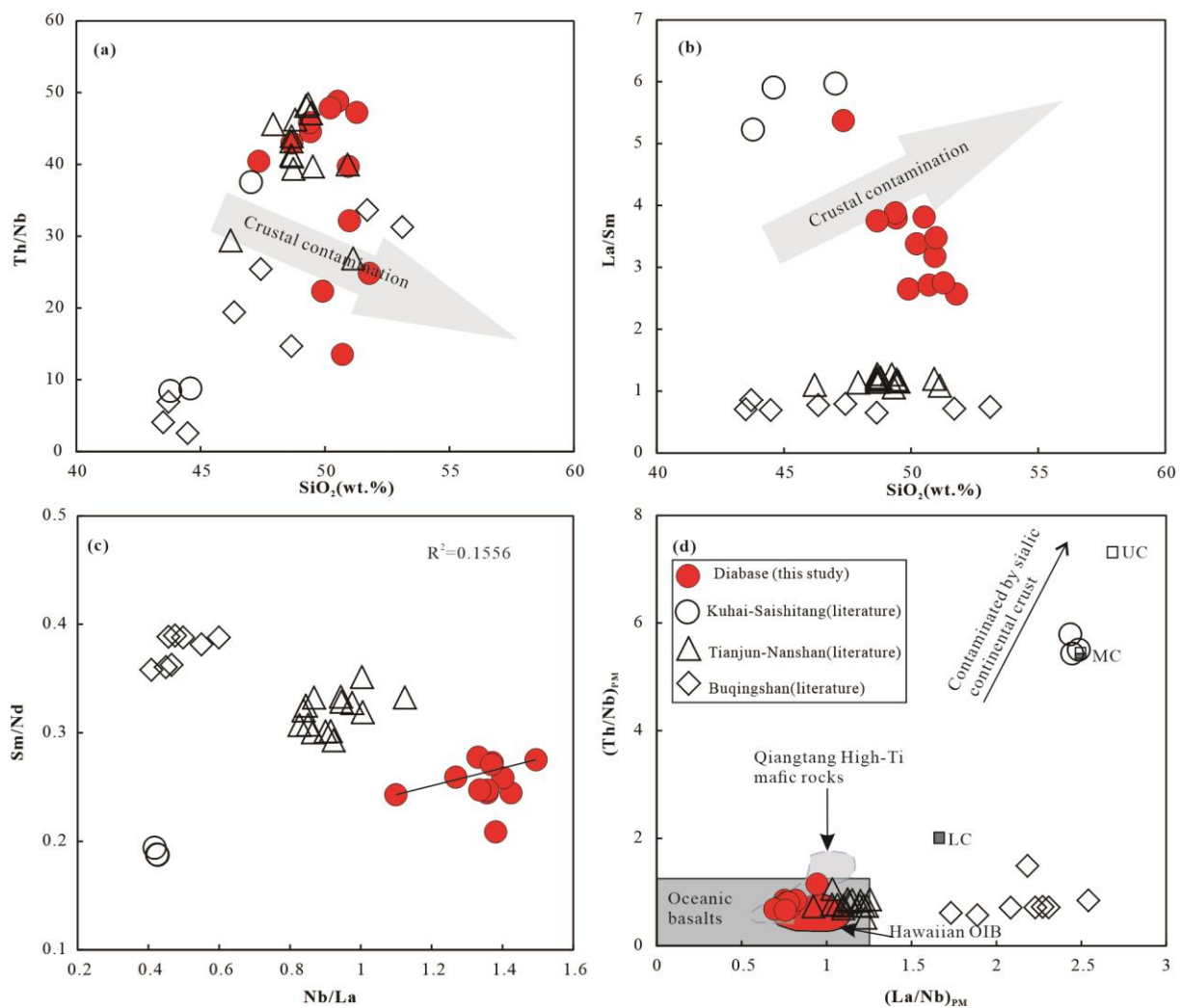


Figure 7. SiO_2 (wt.%) vs. Th/Nb (a), SiO_2 (wt.%) vs. La/Sm (b), Nb/La vs. Sm/Nd (c), and $(\text{La}/\text{Nb})_{\text{PM}}$ vs. $(\text{Th}/\text{Nb})_{\text{PM}}$ (d) plots for testing crustal contamination of Baluogenguole mafic dykes in the ZWLB. Data sources: Subscript PM indicates ratios normalized to primitive mantle values of [64]. UC—upper crust, MC—middle crust, LC—lower crust [76]; Hawaiian OIB [78]; Qiangtang high-Ti mafic rocks [56–58]; oceanic basalts [81].

6.2.2. Fractional Crystallization

The Baluogenguole mafic dykes exhibit low Cr (32.27–312.40 ppm), Ni (31.48–153.04 ppm) contents, as well as low Mg# (39–52). These values are significantly lower than those of primitive basalts (Cr > 1000 ppm, Ni > 400 ppm, ref. [82] and Mg# between 73 and 81, ref. [83]), indicating the extensive fractional crystallization of mafic minerals (e.g., olivine, clinopyroxene) during magmatic evolution. Support for this interpretation comes from the correlation of MgO (wt.%) vs. Ni (ppm) and Cr (ppm) vs. Ni (ppm) (Figure 9a,b). The minor fractionation of olivine is indicated by a decrease in the Ni content, associated with a decrease in the MgO content (Figure 8a), while the fractionation of clinopyroxene is indicated by a decrease in the Ni content associated with a decrease in the Cr content (Figure 8b). Generally, this process of fractional crystallization of a mafic mineral is accompanied by plagioclase crystallization. However, the presence of the subtle Eu anomalies ($\delta\text{Eu} = 0.84\text{--}1.11$) suggests that plagioclase did not separate from the melt as a distinct phase. The various Sr anomalies in some samples (Figure 4d) may reflect the effects of low-grade metamorphism and alteration. The correlation of MgO (wt.%) vs. TiO_2 (wt.%) and MgO (wt.%) vs. TFeO (Figure 9c,d) suggests the fractionation of Fe–Ti oxides.

This interpretation is consistent with mineral phases such as titanomagnetite observed in the photomicrographs.

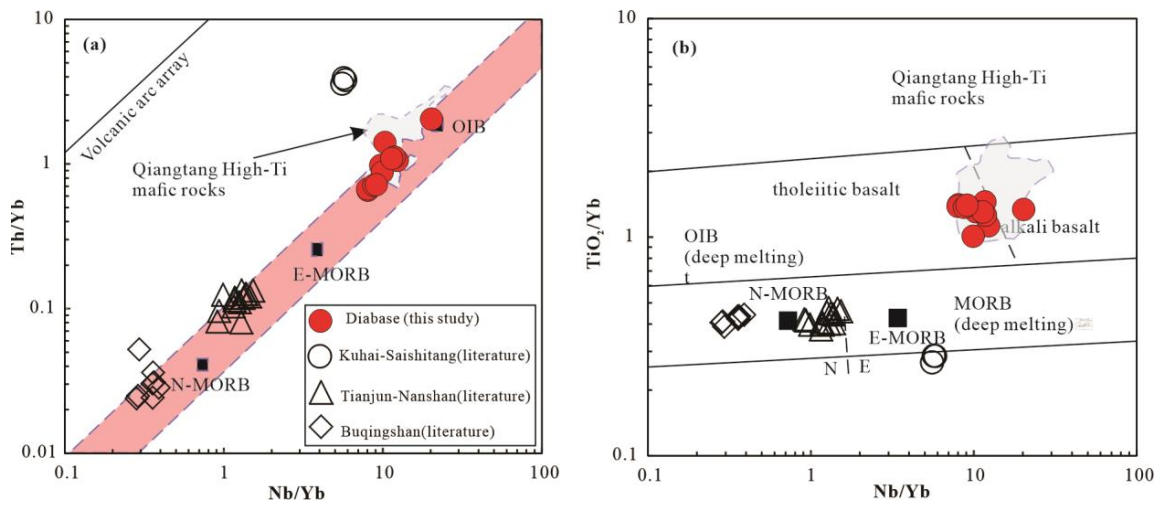


Figure 8. Nb/Yb vs. Th/Yb (a) and Nb/Yb vs. TiO₂/Yb (b) diagrams for Baluogenguole mafic dykes in the ZWLB.

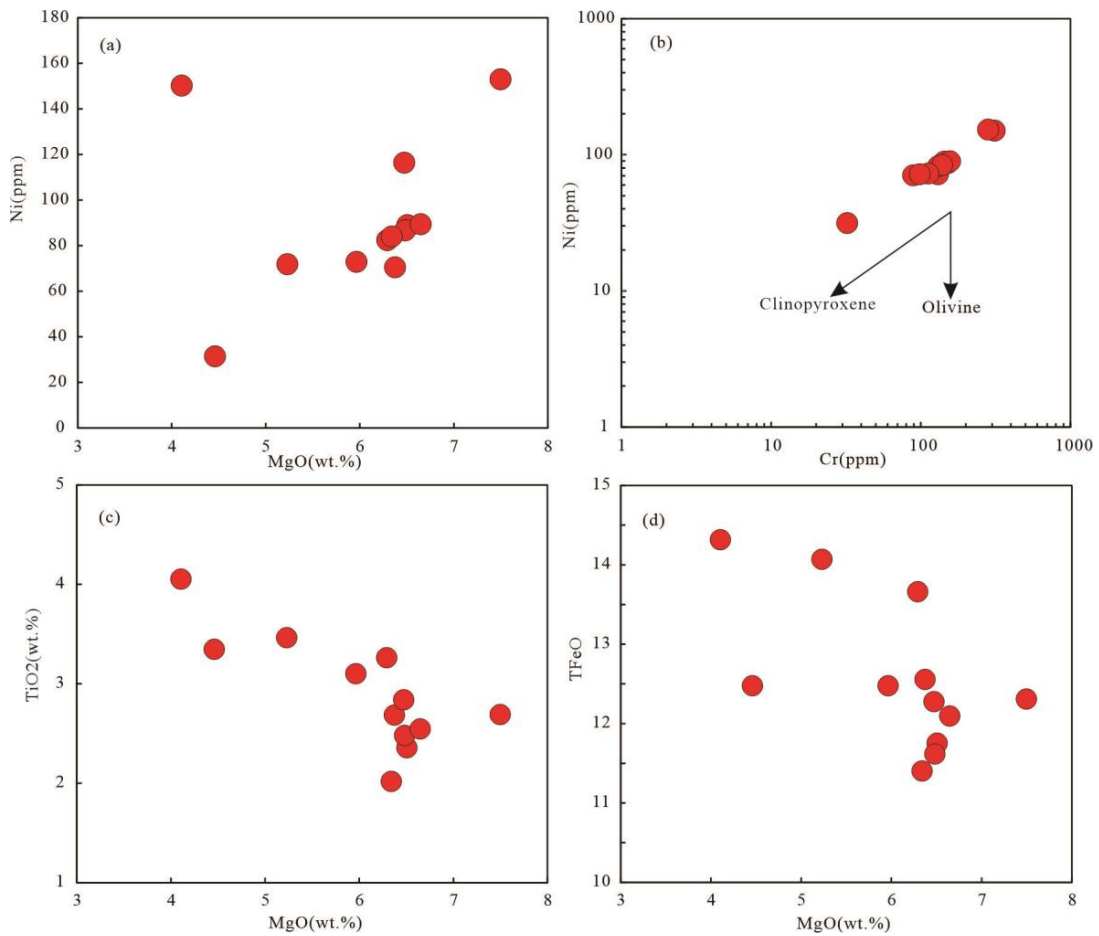


Figure 9. MgO (wt.%) vs. Ni (ppm) (a), Cr (ppm) vs. Ni (ppm) (b), MgO (wt.%) vs. TiO₂ (wt.%) (c) and MgO (wt.%) vs. TFeO (d) plots for testing fractional crystallization of Baluogenguole mafic dykes in the ZWLB.

6.2.3. Magma Source

The Baluogenguole mafic dykes have a high TiO_2 (2.02–4.05 wt.%) content and elevated Nb/Y ratios (0.67–1.76). Their primitive-mantle-normalized trace element patterns are similar to those of the Hawaii OIB-like basalts and Qiangtang high-Ti mafic rocks [57–59,81], with enrichment in HFSEs (Figure 5b). These dykes demonstrate geochemical characteristics of the alkaline basalt series, with negligible crustal contamination. The Nd and Hf isotopes ($\epsilon\text{Nd}(t) = +5.16$ to $+8.47$; $\epsilon\text{Hf}(t) = +1.31$ to $+3.58$; Supplementary Table S3) indicate a mantle source. Furthermore, the samples exhibit high Nb/La ratios (1.10–1.49) and La/Yb ratios (5.87–14.66). In the Nb/Yb vs. Th/Yb and TiO_2/Yb diagrams (Figure 9a,b), the samples are plotted within the OIB field and Qiangtang high-Ti mafic rock field, suggesting that the Baluogenguole mafic dykes originated from a mantle source similar to both OIB and the Qiangtang high-Ti mafic rocks, likely associated with mantle plume activity.

The source characteristics and melting depth can be inferred using the REE abundances and ratios of primary basalts (e.g., [84,85]). In the case of the samples from Baluogenguole mafic rocks, the fractional crystallization of olivine and clinopyroxene occurred without significant crustal contamination. Hence, it is essential to assess the impact of fractional crystallization (olivine and clinopyroxene) on REEs. REEs and yttrium often possess larger ionic radii and/or higher charges compared to the cations commonly present in olivine and clinopyroxene [86]. This property renders them less compatible with these minerals, causing them to concentrate in the melt during the magma's evolution. Consequently, these REE ratios can serve as indicators to evaluate the mantle source characteristics and the depth of melting in Baluogenguole mafic rocks.

The Baluogenguole mafic dykes have relatively low $(\text{Yb}/\text{Sm})_{\text{PM}}$ and $(\text{Tb}/\text{Yb})_{\text{PM}}$ ratios. In the $(\text{Yb}/\text{Sm})_{\text{PM}}$ vs. $(\text{Tb}/\text{Yb})_{\text{PM}}$ diagram, the samples fall within the mantle source region, where garnet peridotite contributes approximately 50%, and low-degree melting (5%–10%) is required (Figure 10a, [87]). The slightly fractionated HREE patterns (Figure 6a) and the relatively high La/Sm and Sm/Yb ratios (Figure 10b), along with their low Ce/Y (1.13–2.49) and moderate Dy/Yb (2.08–2.27) ratios (Supplementary Table S1), support the occurrence of low-degree melting in the spinel–garnet transition zone at depths of approximately 75 km [88].

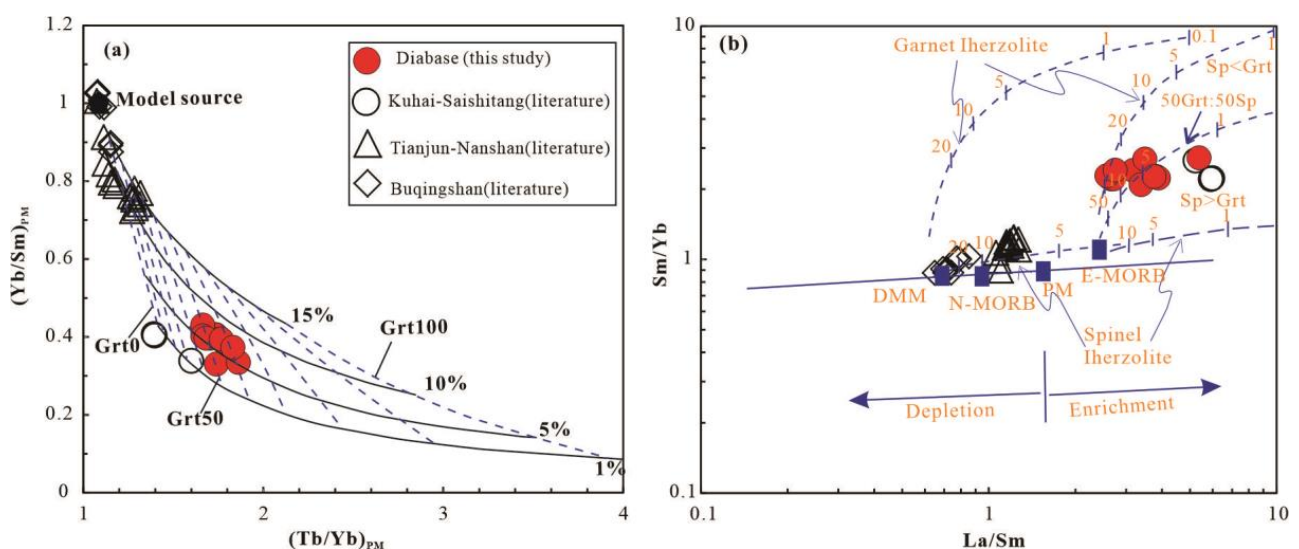


Figure 10. Plots of $(\text{Yb}/\text{Sm})_{\text{PM}}$ vs. $(\text{Tb}/\text{Yb})_{\text{PM}}$ (a) and Sm/Yb vs. La/Sm (b). In (a), the grid shows the range of model melt compositions by different proportions (1%, 5%, 10%, and 15%) of the partial melting of the model source; the proportions of melt contribution from garnet facies peridotite (Grt) are shown by the dashed blue lines, e.g., Grt0 represents the melt from spinel peridotite; the constant melt fraction is indicated by the black lines. Details of model source and model curves are from [87]. In (b), the melting curves are from [84] obtained using the non-modal batch melting equations of [89].

Melt curves are drawn for spinel–lherzolite with mode and melt mode of $ol_{0.530} + opx_{0.270} + cpx_{0.170} + sp_{0.030}$ and $ol_{0.060} + opx_{0.280} + cpx_{0.670} + sp_{0.110}$; respectively [90] and for garnet–lherzolite with mode and melt mode of $ol_{0.600} + opx_{0.200} + cpx_{0.100} + grt_{0.100}$ and $ol_{0.030} + opx_{0.160} + cpx_{0.880} + grt_{0.090}$; respectively [91]; numbers along lines represent degrees of partial melting. Abbreviations: DMM: Depleted MORB Mantle; PM: primitive mantle; N-MORB: normal mid-ocean ridge basalt; E-MORB: enriched mid-oceanic ridge basalt; Grt: garnet; Sp: spinel.

6.3. Tectonic Implications

6.3.1. Tectonic Setting

Mafic dykes are important not only for tracing mantle sources but also for determining their tectonic settings [17,92,93]. Our data from the Baluogenguole mafic dykes display relatively higher Nb, Ta, and TiO_2 contents than those of arc-related basalts in subduction settings [94,95]. The dykes have Zr concentrations (314–351 ppm) and Zr/Y ratios (5.33–6.10) comparable to within-plate basalts (Figure 11a, ref. [96]). On the Ti/100–Zr–3Y and Hf/3–Th–Ta triangle diagram, they lie in the within-plate alkali basalt field (Figure 11b,c, ref. [96,97]). On the Y/15–La/10–Nb/8 (Cabanis and Lecolle, 1989) discrimination diagrams, the samples are plotted in the continental rift alkaline basalt fields (Figure 11d, ref. [98]). These diagrams uniformly indicate that the Baluogenguole mafic dykes formed in an intraplate setting, resembling the Qiangtang high-Ti mafic rocks, which are thought to have formed in a continental rift setting [57,58]. Therefore, we suggest that the Baluogenguole mafic dykes were derived from a continental rift setting.

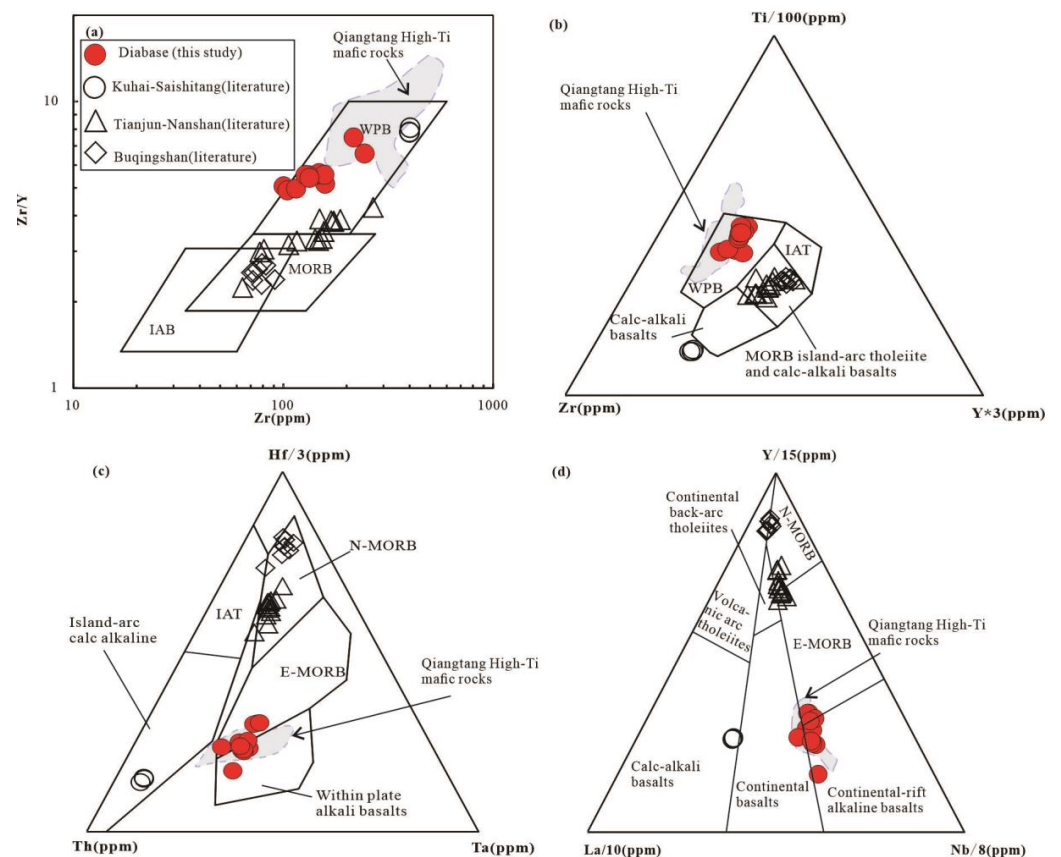


Figure 11. Plots of (a) Zr/Y vs. Zr (after [96]), (b) Ti/100–Zr–3Y (after [96]), (c) Hf/3–Th–Ta (after [97]), and (d) Y/15–La/10–Nb/8 (after [98]) for the Early Permian Baluogenguole mafic dykes in western ZWLB. In (a), WPB: within plate basalts; MORB: mid-ocean ridge basalt; IAB: island arc basalts; IAT: island arc tholeiite.

6.3.2. The Most Distant North Branch of the East Paleo-Tethys Ocean in the ZWLB

There are two main views on the tectonic–magmatic evolution process of the late Paleozoic to Mesozoic in the ZWLB: one is that the ZWLB is a continental rift of the Carboniferous–Permian system [6,7,29], and the Hercyn–Indosinian magmatic rocks in the eastern part of the ZWLB are the result of the northward subduction of the Paleo-Tethyan Ocean [11]. Another view is that there is a narrow ocean basin in the ZWLB, which has undergone a complete process of breakup, subduction, and collision [2,8,9,12,14].

The ZWLB is situated in the northern margin of the Qaidam Basin; Fu [8] proposed that the ZWLB is an early Paleozoic to early Mesozoic composite orogen formed after the closure of the Proto- to Paleo-Tethys oceans. Following the subduction–collision of the Proto-Tethyan Ocean in the early Paleozoic, the Devonian tectonic setting of the ZWLB and the northern margin of the Qaidam Basin is predominantly characterized by post-orogenic extension [12,99,100] (Figure 12a). This extension process has resulted in hornblende gabbro (416 ± 5 Ma, U-Pb age) in the Chahano area [101], A2-type granite (413 ± 3 Ma, U-Pb age) in the Wulan area [12], and the Maoniushan Formation molasse (409 Ma) [102]. These formations indicate that the ZWLB may have been initially rifted since the Early Devonian. Subsequently, the occurrence of Middle and Late Devonian bimodal volcanic rocks (369–396 Ma, U-Pb age) [103], mafic–ultramafic dykes in the Dulan and Xitieshan area (360–392 Ma, U-Pb age) [104], and the occurrence of Lalongwa mafic dykes (LLW) (393.5 ± 3.0 Ma, $^{40}\text{Ar}/^{39}\text{Ar}$ age) [105] in the Kuhai–Saishitang Tectonic Belt, indicate further extension and suggest that breakup is occurring between the southeast ZWLB and the Animaqing Belt. The East Kunlun tectonic belt also exhibits numerous Devonian extensional records, such as Xiarihamu mafic–ultramafic rocks (U-Pb age 431–411 Ma, ref. [106]), Yugusayi hornblende gabbro (U-Pb age 405 Ma, ref. [107]), and Lalingzhuo A2-type granite (U-Pb age 396 ± 2 Ma, ref. [108]). These formations represent the initiation of continental rifts at the onset of the Paleo-Tethyan Ocean.

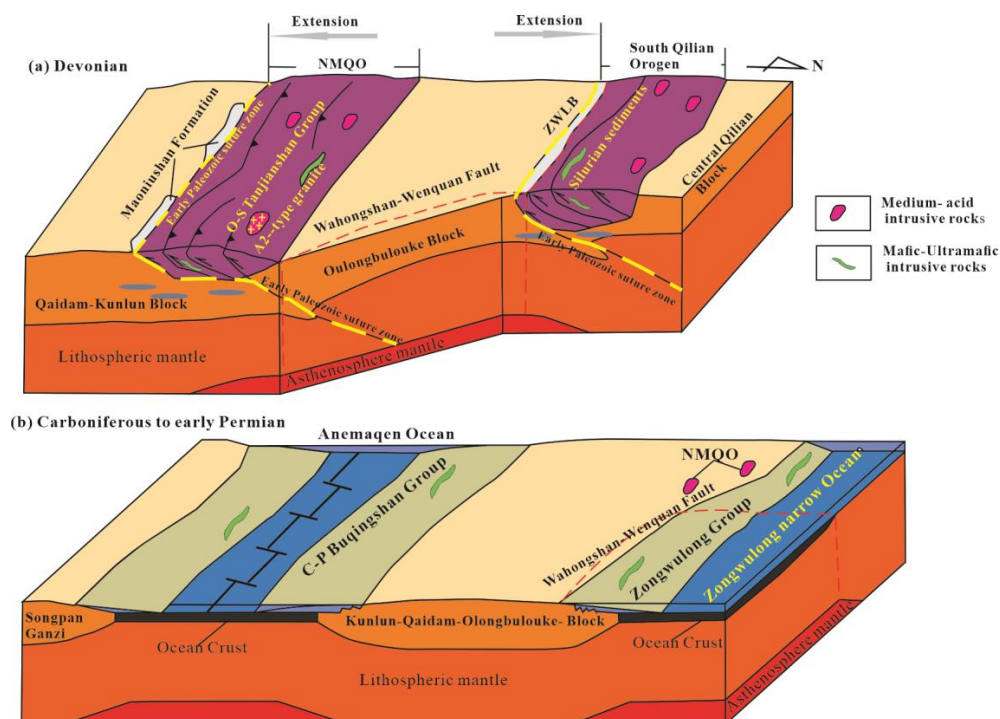


Figure 12. Schematic diagrams illustrating the formation process of the late Paleozoic Zongwulong narrow ocean. NMQO: northern margin of Qaidam Orogen; O-S: Ordovician to Silurian. The Devonian tectonic setting of the ZWLB and the northern margin of the Qaidam Basin is predominantly characterized by post-orogenic extension (a); the Zongwulong narrow ocean formed in the Carboniferous to early Permian, synchronously with the Anemaqen Ocean (b).

As extension continued, the oceanic crust of the Paleo-Tethyan Ocean began to develop (Figure 12b). In the ZWLB, the 318 to 331 Ma Tianjunnanshan N-MORB ophiolitic mélanges [2,8], consistent with the 303 to 353 Ma Buqingshan N-MORB ophiolite mélanges (BQS) in the East Kunlun Orogen, represent the late Paleozoic Anemaqen Paleo-Tethyan oceanic crust [109]. Additionally, 361 ± 4 Ma [103] to 369 ± 1 Ma [5] Kuhai–Saishitang ophiolitic mélanges in the Elashan tectonic belt also evolved synchronously with the Paleo-Tethyan Ocean crust of the Anemaqen region. This information suggests that the late Paleozoic Zongwulong narrow ocean basin evolved synchronously with the Anemaqen Paleo-Tethyan Ocean crust and was linked to the Anemaqen Ocean by the Kuhai–Saishitang ocean–continental transition area [1]. We consider that the Zongwulong narrow ocean may be the most distant northern branch of the East Paleo-Tethys Ocean.

However, the Zongwulong narrow ocean only developed in the eastern part, while there are no relevant records associated with the ocean in the western part. The mafic dykes (U-Pb age, 289 ± 1 Ma) in the Baluogenguole area of the western part exhibited intraplate alkaline basalt, which indicates that the western part was still an intraplate setting when the Tianjunnanshan oceanic crust developed in the eastern part. In fact, there is a significant difference in the rock compositions between the eastern and western parts of the ZWLB, with the Wahongshan Fault serving as the boundary. In the western ZWLB, there are no late Paleozoic to early Mesozoic arc-type granitoids and ophiolites, or their rock fragments. The Turgendaban Formation exhibits flysch sedimentary characteristics, and the restricted Longwuhe Formation displays molasse unit features [44,45]. The detrital zircon ages of the Triassic Longwuhe Formation in the Haitoutala area are almost blank between 408 and 249 Ma, suggesting that the sediments of the Longwuhe Formation in the western part do not contain magmatic records related to the closure of the late Paleozoic Paleo-Tethys Ocean [45]. In the eastern ZWLB, the Longwuhe Formation is extensively distributed and resembles the Longwuhe Formation of the West Qinling Orogen, showing typical flysch clastic rock deposition. Ophiolites are present in the Tianjunnanshan area, and late Paleozoic to early Mesozoic granitoids, associated with oceanic subduction and continental collision, are widespread. The detrital zircon ages of the Zongwulong Group in the Shengge area provide a complete record from 404 to 206 million years ago [110], aligning well with the late Paleozoic to early Mesozoic granitoids linked to Paleo-Tethys oceanic subduction and continental collision.

Therefore, we believe that the initial breakup of the ZWLB occurred in the Early Devonian to Early Carboniferous, and the intra-continental breakup continued in the Late Carboniferous–Early Permian. The eastern ZWLB developed ophiolites with N-MORB chemical characteristics similar to the Buqingshan–Anemaqen ophiolite, indicating that the oceanic crust of the Paleo-Tethyan Ocean began to develop in the eastern part, possibly linked to the Anemaqen Paleo-Tethys Ocean by the Kuhai–Saishitang ocean–continental transition area. At the same time, mafic dykes with intraplate setting characteristics developed in the western ZWLB, representing a continental rift setting. The ZWLB likely experienced a continental rift in the western part and a narrow oceanic environment in the eastern part in the late Paleozoic.

7. Conclusions

1. The zircon U-Pb dating of the newly discovered Baluogenguole mafic dykes yielded ages of 289.3 ± 1.2 Ma, and are interpreted as existing in the age of intrusion.
2. The Baluogenguole mafic dykes underwent negligible crustal contamination, and experienced extensive fractional crystallization of olivine, clinopyroxene, and Fe-Ti oxides but not of plagioclase. They were produced from the spinel–garnet transition zone at depths of ~ 75 km, and garnet facies low-degree melting (5–10%).
3. The Baluogenguole mafic dykes were formed in a continental rift setting. Combined with the regional geological data, the ZWLB likely experienced a continental rift in the west and a narrow oceanic environment in the east, possibly making it the most distant north branch of the East Paleo-Tethys Ocean.

Supplementary Materials: The following supporting information can be downloaded at <https://www.mdpi.com/article/10.3390/min14050473/s1>. Table S1: Whole-rock major (%) and trace element (ppm) compositions of Baluogenguole mafic dykes in the ZWLB. Table S2: LA-ICM-MS zircon U–Pb data of Baluogenguole mafic dykes in the ZWLB. Table S3: Whole-rock Sr–Nd isotopic compositions of the Baluogenguole mafic dykes in the ZWLB. Table S4: LA-ICM-MS zircon Lu–Hf isotopic data of Baluogenguole mafic dykes in the ZWLB.

Author Contributions: Conceptualization, M.C. and C.-L.X.; methodology, W.-T.Z.; software, C.-J.X.; validation, M.C., Y.-H.W. and T.P. formal analysis, M.C. and W.-T.Z.; investigation, T.P.; resources, W.-T.Z.; data curation, M.C.; writing—original draft preparation, T.P. and Y.-H.W.; writing—review and editing, C.-J.X.; visualization, T.P. and B.-Z.W.; supervision, T.P. and Y.-H.W.; project administration, T.P. and Y.-H.W.; funding acquisition. All authors have read and agreed to the published version of the manuscript.

Funding: The Second Tibetan Plateau Scientific Expedition and Research Program (STEP, Grant No. 2019QZKK0806); geological survey project of China Geological Survey (DD20220979).

Data Availability Statement: All data supporting the results of this study can be found in the figures and Supplementary Materials submitted to the journal.

Acknowledgments: We thank the Nanjing Hongchuang Geological Exploration Technology Service for their laboratory assistance.

Conflicts of Interest: The authors declare that they have no conflicts of interest.

References

1. Guo, A.L.; Zhang, G.W.; Sun, Y.G.; Cheng, S.Y.; Qiang, J. Sr–Nd–Pb isotopic geochemistry of Late–Paleozoic mafic volcanic rocks in the surrounding areas of the Gonghe basin, Qinghai Province and geological implications. *Acta Petrol. Sin.* **2007**, *23*, 747–754. (In Chinese with English abstract)
2. Wang, Y.Z.; Bai, Y.S.; Lu, H.L. Geological characteristics of Tianjunnanshan ophiolite in Qinghai and its forming environment. *Qinghai Geol.* **2001**, *29*, 29–35. (In Chinese with English abstract)
3. Chen, L.; Sun, Y.; Pei, X.; Gao, M.; Feng, T.; Zhang, Z.; Chen, W. Northernmost paleo-tethyan oceanic basin in Tibet: Geochronological evidence from $40\text{Ar}/39\text{Ar}$ age dating of Duren'ngoi ophiolite. *Chin. Sci. Bull.* **2001**, *46*, 1203–1205. [[CrossRef](#)]
4. Yue, Y.; Dong, Y.; Sun, S.; He, D.; Hui, B.; Ren, X.; Zhang, B.; He, W. Mafic-ultramafic rocks in the Buqingshan Complex of the East Kunlun Orogen, northern Tibetan Plateau: Remnants of the Paleo-Tethys Ocean. *Int. Geol. Rev.* **2022**, *64*, 3149–3170. [[CrossRef](#)]
5. Wang, B.Z.; Zhang, Z.Y.; Zhang, S.Q.; Zhu, Y.T.; Cao, S.X. Geological features of lower Paleozoic ophiolite in Kuhai–Saishitang region, eastern section of Eastern Kunlun. *Earth Sci. J. China Univ. Geosci.* **2000**, *25*, 592–598. (In Chinese with English abstract)
6. Li, P.A.; Nie, S.R. Structural characteristics of Zongwulong rift. *Geol. Qinghai* **1982**, 65–76. (In Chinese with English abstract)
7. Bureau of Geology and Mineral Resources Qinghai Province (BGMQ). *Regional Geology of Qinghai Province*; Geological Publishing House: Beijing, China, 1991. (In Chinese)
8. Fu, C.L.; Yan, Z.; Xiao, W.J.; Wang, B.Z.; Niu, M.L.; Yu, L.J. Identification and geological significance of the Early Paleozoic Tianjunnanshan remnant ocean basin in the Zongwulong belt, NE Tibetan Plateau. *Acta Petrol. Sin.* **2021**, *37*, 2401–2418. (In Chinese with English abstract)
9. Guo, A.L.; Zhang, G.W.; Qiang, J.; Sun, Y.G.; Li, G.; Yao, A.P. Indosinian Zongwulong orogenic belt on the northeastern margin of the Qinghai–Tibet Plateau. *Acta Petrol. Sin.* **2009**, *25*, 1–12. (In Chinese with English abstract)
10. Peng, Y.; Ma, Y.S.; Liu, C.L.; Li, Z.X.; Sun, J.P.; Shao, P.C. Geological characteristics and tectonic significance of the Indosinian granodiorites from the Zongwulong Belt in North Qaidam. *Earth Sci. Front.* **2016**, *23*, 206–221. (In Chinese with English abstract)
11. Niu, M.L.; Zhao, Q.Q.; Wu, Q.; Li, X.C.; Yan, Z.; Li, J.L.; Yuan, X.Y. Magma mixing identified in the Guokeshan pluton, northern margin of the Qaidam basin: Evidences from petrography, mineral chemistry, and whole-rock geochemistry. *Acta Petrol. Sin.* **2018**, *34*, 1991–2016. (In Chinese with English abstract)
12. Wu, C.; Wu, D.; Mattinson, C.; Lei, M.; Chen, H. Petrogenesis of granitoids in the Wulan area: Magmatic activity and tectonic evolution in the North Qaidam, NW China. *Gondwana Res.* **2018**, *67*, 147–171. [[CrossRef](#)]
13. Chen, M.; Xue, C.J.; Xue, W.W.; Zhao, W.T. Discovery and Geological significance of Xuji diorite in Zongwulong Belt at the northern margin of Qaidam Basin. *Acta Petrol. Et Mineralogica* **2020**, *39*, 552–568. (In Chinese with English abstract)
14. Zou, F.; Wu, C.; Deng, L.; Gao, D.; Gao, Y. Petrological and geochemical constraints on the petrogenesis of granitoids in the Gonghe geothermal basin, western Qinling (China). *Appl. Geochem.* **2022**, *136*, 105176. [[CrossRef](#)]
15. Wang, B.Z.; Han, J.; Xie, X.L.; Chen, J.; Wang, T.; Xue, W.W.; Li, S.P. Discovery of the Indosinian (Beryl-bearing) Spodumene Pegmatitic Dike Swarm in the Chakaibeishan Area in the Northeastern Margin of the Tibetan Plateau: Implications for Li–Be Mineralization. *Geotecton. Et Metallog.* **2020**, *44*, 69–79. (In Chinese with English abstract)

16. Liu, J.D.; Li, S.P.; Li, W.F.; Cao, J.S.; Gu, P.Y.; Cao, H.W.; Zheng, Y.; Wang, C.T.; Jin, T.T.; Zhang, X.Y. Discovery of Spodumene Granite-Pegmatite Dike Group in Northern Hongling Area, Northeastern Margin of Qinghai-Tibet Plateau and Its Prospecting Prospect. *Geology in China*. 2023. Available online: <https://kns.cnki.net/kcms2/detail/11.1167.p.20230614.1321.002.html> (accessed on 15 June 2023). (In Chinese with English abstract)
17. Halls, H.C. The importance and potential of mafic dyke swarms in studies of geodynamic processes. *Geosci. Can.* **1982**, *9*, 145–154.
18. Liu, S.; Feng, C.X.; Jahn, B.M.; Hu, R.Z.; Gao, S.; Coulson, I.M.; Feng, G.; Lai, S.; Yang, C.; Yang, Y. Zircon U-Pb age, geochemical, and Sr-Nd-Hf isotopic constraints on the origin of mafic dykes in the Shanxi Province, North China Craton, China. *Lithos* **2013**, *175–176*, 244–254. [[CrossRef](#)]
19. Xu, Z.Q.; Yang, J.S.; Li, H.B.; Yao, J.X. The early Paleozoic terrane framework and the formation of the high-pressure (HP) and ultrahigh pressure (UHP) metamorphic belts at the Central Orogenic Belt (COB). *Acta Geologica Sin.* **2006**, *80*, 1793–1806. (In Chinese with English abstract)
20. Dong, Y.; Sun, S.; Santosh, M.; Zhao, J.; Sun, J.; He, D.; Shi, X.; Hui, B.; Cheng, C.; Zhang, G. Central China Orogenic Belt and amalgamation of East Asian continents. *Gondwana Res.* **2021**, *100*, 131–194. [[CrossRef](#)]
21. Yin, H.F.; Zhang, K.X. Characteristics of the Eastern Kunlun Orogenic Belt. *J. China Univ. Geosci.* **1997**, *4*, 339–342. (In Chinese with English abstract)
22. Yang, J.S.; Ma, C.Q.; Wu, C.L.; Zhang, J.X.; Wang, Z.Q.; Wang, G.C.; Zhang, H.F.; Dong, Y.-P.; Lai, S.C. Compound orogeny and scientific problems concerning the Central Orogenic Belt of China. *Geol. China* **2010**, *37*, 1–11. (In Chinese with English abstract)
23. Yan, Z.; Aitchison, J.; Fu, C.L.; Guo, X.Q.; Niu, M.L.; Xiao, W.J.; Li, J. Hualong Complex, South Qilian terrane: U-Pb and Lu-Hf constraints on Neoproterozoic micro-continental fragments accreted to the northern Proto-Tethyan margin. *Precambrian Res.* **2015**, *216*, 65–82. [[CrossRef](#)]
24. Dong, Y.; Santosh, M. Tectonic architecture and multiple orogeny of the Qinling Orogenic Belt, Central China. *Gondwana Res.* **2015**, *29*, 1–40. [[CrossRef](#)]
25. Zhang, J.; Yu, S.; Mattinson, C. Early Paleozoic polyphase metamorphism in northern Tibet, China. *Gondwana Res.* **2017**, *41*, 267–289. [[CrossRef](#)]
26. Li, R.B.; Pei, X.Z.; Li, Z.C.; Pei, L.; Chen, G.C.; Wei, B.; Chen, Y.; Liu, C.; Wang, M. Cambrian (~510 Ma) ophiolites of the East Kunlun orogen, China: A case study from the Acite ophiolitic tectonic mélange. *Int. Geol. Rev.* **2018**, *60*, 2063–2083. [[CrossRef](#)]
27. Pei, X.Z.; Li, R.B.; Li, Z.C.; Liu, C.J.; Chen, Y.X.; Pei, L.; Wang, M. Composition feature and formation process of Buqingshan composite accretionary mélange belt in southern margin of East Kunlun Orogen. *Earth Sci.* **2018**, *43*, 4498–4520. (In Chinese with English abstract)
28. Dong, J.; Song, S.; Su, L.; Allen, M.B.; Li, Y.; Wang, C. Early Devonian mafic igneous rocks in the East Kunlun Orogen, NW China: Implications for the transition from the Proto- to Paleo-Tethys oceans. *Lithos* **2020**, *376–377*, 105771. [[CrossRef](#)]
29. Pan, G.; Wang, L.; Li, R.; Yuan, S.; Ji, W.; Yin, F.; Zhang, W.; Wang, B. Tectonic evolution of the Qinghai-Tibet Plateau. *J. Asian Earth Sci.* **2012**, *53*, 3–14. [[CrossRef](#)]
30. Dai, S.; Ma, X.; Zhao, Z.; Fan, X.; Wang, Y.; Wang, Z.; Zhang, X.; Cai, L.; Deng, W.; Hou, X.; et al. Jurassic Evolution of the Dunhuang Basin and Its Implications for the Early History of the Altyn Tagh Fault, Northeast Tibet Plateau. *Tectonics* **2023**, *42*, e2022TC007620. [[CrossRef](#)]
31. Wu, C.; Yin, A.; Zuzva, A.V.; Zhang, J.; Liu, W.; Ding, L. Pre-Cenozoic geologic history of the central and northern Tibetan Plateau and the role of Wilson cycles in constructing the Tethyan orogenic system. *Lithosphere* **2016**, *8*, 254–292. [[CrossRef](#)]
32. Chen, N.S.; Zhang, L.; Sun, M.; Wang, Q.Y.; Kusky, T.M. U-Pb and Hf isotopic compositions of detrital zircons from the paragneisses of the Quanji Massif, NW China: Implications for its early tectonic evolutionary history. *J. Asian Earth Sci.* **2012**, *54–55*, 110–130. [[CrossRef](#)]
33. Lu, S.N.; Wang, H.C.; Li, H.K.; Yuan, G.B.; Xin, H.T.; Zheng, J.K. Redefinition of the “Dakendaban Group” on the northern margin of the Qaidam basin. *Geol. Bull. China* **2002**, *21*, 19–23. (In Chinese with English abstract)
34. Hao, G.J.; Lu, S.N.; Xin, H.T.; Wang, H.C. The constitution and importance geological events of Pre-Devonian in the Dulan, Qinghai. *J. Jilin Univ. (Earth Sci. Ed.)* **2004**, *34*, 495–501, 516 (In Chinese with English abstract).
35. Wang, H.C.; Li, H.K.; Lu, S.N.; Yuan, G.B.; Xin, H.T. Geological characteristics and tectonic setting of the Dakendaba group in Iqe area, northern margin of Qaidam Basin. *Geol. Surv. Res.* **2006**, *29*, 253–262. (In Chinese with English abstract)
36. Chen, N.S.; Wang, Q.Y.; Chen, Q.; Li, X.Y. Components and metamorphism of the basements of the Qaidam and Oulongbuluke micro-continental blocks, and a tentative interpretation of paleocontinental evolution in NW-Central China. *Earth Sci. Front.* **2007**, *14*, 43–55. (In Chinese with English abstract)
37. Sun, J.P.; Chen, S.Y.; Peng, Y.; Shao, P.C.; Ma, S.; Liu, J. Research on Northern Qaidam tectonic attributes during Devonian. *J. China Univ. Pet.* **2015**, *39*, 23–30. (In Chinese with English abstract)
38. Wang, M.; Pei, X.; Li, R.; Pei, L.; Li, Z.; Liu, C.; Xu, L.; Lin, H. Timing of Transition from Proto- to Paleo-Tethys: Evidence from the Early Devonian Bimodal Volcanics in the North Qaidam Tectonic Belt, Northern Tibetan Plateau. *Minerals* **2023**, *13*, 532. [[CrossRef](#)]
39. Wang, T.; Zhou, Y.; He, W.; He, L.; Cheng, X.; Deng, X.; Zhang, D.; Wei, B.; Jiang, N.; Wu, H. Provenance change in Carboniferous-early Permian sedimentary successions in the North Qaidam tectonic belt, northern Tibetan Plateau: Implications for the Kunlun oceanic plate subduction process. *J. Asian Earth Sci.* **2022**, *240*, 105434. [[CrossRef](#)]

40. Liu, J.; Qian, T. Discovery of Permian tuff from the northern margin of the Qaidam Basin and its geological implications. *J. Geomech.* **2023**, *29*, 290–300. (In Chinese with English abstract)
41. Tung, K.; Yang, H.-J.; Yang, H.-Y.; Liu, D.; Zhang, J.; Wan, Y.; Tseng, C.-Y. SHRIMP U-Pb geochronology of the zircons from the Precambrian basement of the Qilian Block and its geological significances. *Chin. Sci. Bull.* **2007**, *52*, 2687–2701. [[CrossRef](#)]
42. Yan, Z.; Fu, C.L.; Aitchison, J.C.; Zhou, R.J.; Buckman, S.; Chen, L. Silurian sedimentation in the South Qilian Belt: Arc-continent collision-related deposition in the NE Tibet Plateau? *Acta Geol. Sin.* **2020**, *94*, 901–913. [[CrossRef](#)]
43. Fu, C.; Yan, Z.; Guo, X.; Niu, M.; Cao, B.; Wu, Q.; Li, X.; Wang, Z. Assembly and dispersal history of continental blocks within the Altun-Qilian-North Qaidam mountain belt, NW China. *Int. Geol. Rev.* **2018**, *61*, 424–447. [[CrossRef](#)]
44. Liu, K.; Li, Z.X.; Shi, X.B.; Wei, X.J.; Ren, Z.Q.; Yang, X.Q.; Bo, P. Late Hercynian-Indosinian denudation and uplift history in the eastern Qaidam Basin: Constraints from multiple thermometric indicators and sedimentary evidences. *Chin. J. Geophys.* **2020**, *64*, 1403–1421. (In Chinese with English abstract)
45. Zhao, W.T.; Liu, X.F.; Chen, M.; Xue, C.J. Detrital zircon characteristics of the Triassic Longwuhe Formation in the western segment of the Zongwulong Belt and its tectonic significance. *Acta Petrol. Et Mineralogica* **2022**, *41*, 569–591. (In Chinese with English abstract)
46. Peng, Z.J.; Wu, P.D.; Liu, S.B.; Zhang, P. An analysis of sediments characteristics of Early-Middle Traissic Longwuhe Formation from Guomaying area in Guinan County, Qinghai Province. *Geol. Bull. China* **2016**, *35*, 1506–1511. (In Chinese with English abstract)
47. Liu, S.; Hu, R.Z.; Gao, S.; Feng, C.X.; Qi, L.; Zhong, H.; Xiao, T.; Qi, Y.; Wang, T.; Coulson, I.M. Zircon U-Pb geochronology and major, trace elemental and Sr-Nd-Pb isotopic geochemistry of mafic dykes in western Shandong Province, east China: Constrains on their petrogenesis and geodynamic significance. *Chem. Geol.* **2008**, *255*, 329–345. [[CrossRef](#)]
48. Black, L.P.; Kamo, S.L.; Allen, C.M.; Davis, D.W.; Aleinikoff, J.N.; Valley, J.W.; Mundil, R.; Campbell, I.H.; Korsch, R.J.; Williams, I.S.; et al. Improved ²⁰⁶Pb/²³⁸U microprobe geochronology by the monitoring of a trace-element-related matrix effect; SHRIMP, ID-TIMS, LA-ICPMS, and oxygen isotope documentation for a series of zircon standards. *Chem. Geol.* **2004**, *205*, 115–140. [[CrossRef](#)]
49. Wiedenbeck, M.; Hanchar, J.M.; Peck, W.H.; Sylvester, P.; Valley, J.; Whitehouse, M.; Kronz, A.; Morishita, Y.; Nasdala, L.; Fiebig, J.; et al. Further Characterisation of the 91500 Zircon Crystal. *Geostand. Geoanal. Res.* **2004**, *28*, 9–39. [[CrossRef](#)]
50. Paton, C.; Woodhead, J.D.; Hellstrom, J.C.; Hergt, J.M.; Greig, A.; Maas, R. Improved laser ablation U-Pb zircon geochronology through robust downhole fractionation correction. *Geochem. Geophys. Geosyst.* **2010**, *11*, Q0AA06. [[CrossRef](#)]
51. Ludwig, K.R. *User's Manual for Isoplot/Ex. Version 3. A Geochronological Toolkit for Microsoft Excel*; Berkeley Geochronology Center Special Publication: Berkeley, CA, USA, 2003; p. 4.
52. Liu, Y.; Gao, S.; Hu, Z.; Gao, C.; Zong, K.; Wang, D. Continental and Oceanic Crust Recycling-induced Melt-Peridotite Interactions in the Trans-North China Orogen: U-Pb Dating, Hf Isotopes and Trace Elements in Zircons from Mantle Xenoliths. *J. Pet.* **2009**, *51*, 537–571. [[CrossRef](#)]
53. Sláma, J.; Košler, J.; Condon, D.J.; Crowley, J.L.; Gerdes, A.; Hanchar, J.M.; Horstwood, M.S.A.; Morris, G.A.; Nasdala, L.; Norberg, N.; et al. Plešovice zircon—A new natural reference material for U–Pb and Hf isotopic microanalysis. *Chem. Geol.* **2008**, *249*, 1–35. [[CrossRef](#)]
54. Fourny, A.; Weis, D.; Scoates, J.S. Comprehensive Pb-Sr-Nd-Hf isotopic, trace element, and mineralogical characterization of mafic to ultramafic rock reference materials. *Geochem. Geophys. Geosyst.* **2016**, *17*, 739–773. [[CrossRef](#)]
55. Weis, D. High-precision isotopic characterization of USGS reference materials by TIMS and MC-ICP-MS. *Geochem. Geophys. Geosyst.* **2006**, *7*, Q08006. [[CrossRef](#)]
56. Tanaka, T.; Togashi, S.; Kamioka, H.; Amakawa, H.; Kagami, H.; Hamamoto, T.; Yuhara, M.; Orihashi, Y.; Yoneda, S.; Shimizu, H.; et al. JNdi-1: A neodymium isotopic reference in consistency with LaJolla neodymium. *Chem. Geol.* **2000**, *168*, 279–281. [[CrossRef](#)]
57. Wang, M.; Li, C.; Wu, Y.-W.; Xie, C.-M. Geochronology, geochemistry, Hf isotopic compositions and formation mechanism of radial mafic dikes in northern Tibet. *Int. Geol. Rev.* **2013**, *56*, 187–205. [[CrossRef](#)]
58. Wang, M.; Li, C.; Zeng, X.W.; Li, H.; Fan, J.J.; Xie, C.M.; Hao, Y.J. Petrogenesis of the southern Qiangtang mafic dykes, Tibet: Link to a late Paleozoic mantle plume on the northern margin of Gondwana? *Geol. Soc. Am. Bull.* **2019**, *131*, 1907–1919. [[CrossRef](#)]
59. Xu, W.; Dong, Y.; Zhang, X.; Deng, M.; Zhang, L. Petrogenesis of high-Ti mafic dykes from Southern Qiangtang, Tibet: Implications for a ca. 290 Ma large igneous province related to the early Permian rifting of Gondwana. *Gondwana Res.* **2015**, *36*, 410–422. [[CrossRef](#)]
60. Zhang, Z.Y.; Yin, H.F.; Wang, B.Z.; Wang, J.; Zhang, K.X. Presence and evidence of Kuhai-Saishitang branching ocean in copulae between Kunlun-Qinling mountains. *Earth Sci. (J. China Univ. Geosci.)* **2004**, *29*, 691–696. (In Chinese with English abstract)
61. Frey, F.A.; Green, D.H.; Roy, S.D. Integrated Models of Basalt Petrogenesis: A Study of Quartz Tholeiites to Olivine Melilitites from South Eastern Australia Utilizing Geochemical and Experimental Petrological Data. *J. Pet.* **1978**, *19*, 463–513. [[CrossRef](#)]
62. Middlemost, E.A.K. Naming materials in the magma/igneous rock system. *Earth-Sci. Rev.* **1994**, *37*, 215–224. [[CrossRef](#)]
63. Winchester, J.; Floyd, P. Geochemical discrimination of different magma series and their differentiation products using immobile elements. *Chem. Geol.* **1977**, *20*, 325–343. [[CrossRef](#)]
64. Sun, S.S.; McDonough, W.F. Chemical and isotopic systematics of oceanic basalts; implications for mantle composition and processes. In *Magmatism in the Ocean Basins*. Geological Society of London; Saunders, A.D., Norry, M.J., Eds.; Geological Society Publication: London, UK, 1989; pp. 313–345.

65. Tang, Y.-J.; Zhang, H.-F.; Ying, J.-F. Asthenosphere–lithospheric mantle interaction in an extensional regime: Implication from the geochemistry of Cenozoic basalts from Taihang Mountains, North China Craton. *Chem. Geol.* **2006**, *233*, 309–327. [[CrossRef](#)]
66. Zhang, J.-J.; Zheng, Y.-F.; Zhao, Z.-F. Geochemical evidence for interaction between oceanic crust and lithospheric mantle in the origin of Cenozoic continental basalts in east-central China. *Lithos* **2009**, *110*, 305–326. [[CrossRef](#)]
67. Corfu, F.; Hanchar, J.M.; Hoskin, P.W.; Kinny, P. Atlas of zircon textures. *Rev. Mineral. Geochem.* **2003**, *53*, 469–500. [[CrossRef](#)]
68. Wu, Y.; Zheng, Y. Genesis of zircon and its constraints on interpretation of U–Pb age. *Chin. Sci. Bull.* **2004**, *49*, 1554–1569. [[CrossRef](#)]
69. Rubatto, D. Zircon trace element geochemistry: Partitioning with garnet and the link between U–Pb ages and metamorphism. *Chem. Geol.* **2002**, *184*, 123–138. [[CrossRef](#)]
70. Song, S.G.; Niu, Y.; Su, L.; Zhang, C.; Zhang, L.F. Continental orogenesis from ocean subduction, continent collision/subduction, to orogen collapse, and orogeny recycling: The example of the North Qaidam UHPM belt, NW China. *Earth Sci. Rev.* **2014**, *129*, 59–84. [[CrossRef](#)]
71. Yu, S.; Zhang, J.; del Real, P.G.; Zhao, X.; Hou, K.; Gong, J.; Li, Y. The Grenvillian orogeny in the Altun–Qilian–North Qaidam mountain belts of northern Tibet Plateau: Constraints from geochemical and zircon U–Pb age and Hf isotopic study of magmatic rocks. *J. Asian Earth Sci.* **2013**, *73*, 372–395. [[CrossRef](#)]
72. Gibson, I.L.; Kirkpatrick, R.J.; Emmerman, R.; Schmincke, H.; Pritchard, G.; Oakley, P.J.; Thorpe, R.S.; Marriner, G.F. The trace element composition of the lavas and dikes from a 3-km vertical section through the lava pile of eastern Iceland. *J. Geophys. Res.* **1982**, *87*, 6532–6546. [[CrossRef](#)]
73. Wood, D.A.; Joron, J.-L.; Treuil, M. A re-appraisal of the use of trace elements to classify and discriminate between magma series erupted in different tectonic settings. *Earth Planet. Sci. Lett.* **1979**, *45*, 326–336. [[CrossRef](#)]
74. Meng, L.; Li, Z.-X.; Chen, H.; Li, X.-H.; Wang, X.-C. Geochronological and geochemical results from Mesozoic basalts in southern South China Block support the flat-slab subduction model. *Lithos* **2012**, *132–133*, 127–140. [[CrossRef](#)]
75. Gao, P.; Zheng, Y.-F.; Yakymchuk, C.; Zhao, Z.-F.; Meng, Z.-Y. The Effects of Source Mixing and Fractional Crystallization on the Composition of Eocene Granites in the Himalayan Orogen. *J. Pet.* **2021**, *62*, egab037. [[CrossRef](#)]
76. Rudnick, R.L.; Gao, S. Composition of the Continental Crust. In *Treatise on Geochemistry*; Rudnick, R.L., Holland, H.D., Turekian, K.K., Eds.; Elsevier: Amsterdam, The Netherlands, 2003; Volume 3, pp. 1–64.
77. Condie, K.C. Chemical composition and evolution of the upper continental crust: Contrasting results from surface samples and shales. *Chem. Geol.* **1993**, *104*, 1–37. [[CrossRef](#)]
78. Frey, F.A.; Weis, D.; Borisova, A.Y.; Xu, G. Involvement of Continental Crust in the Formation of the Cretaceous Kerguelen Plateau: New Perspectives from ODP Leg 120 Sites. *J. Pet.* **2002**, *43*, 1207–1239. [[CrossRef](#)]
79. Wanless, V.D.; Garcia, M.O.; Rhodes, J.M.; Weis, D.; Norman, M.D. Shield-stage alkali volcanism on Mauna Loa Volcano, Hawaii. *J. Volcanol. Geotherm. Res.* **2006**, *151*, 141–155. [[CrossRef](#)]
80. Fitton, J.G. Coupled molybdenum and niobium depletion in continental basalts. *Earth Planet. Sci. Lett.* **1995**, *136*, 715–721. [[CrossRef](#)]
81. Palme, H.; O’Neill, H.S.C. Cosmochemical estimates of mantle composition. *Treatise Geochem.* **2003**, *2*, 1–38.
82. Wilson, M. *Igneous Petrogenesis: A Global Tectonic Approach*; Unwin Hyman: London, UK, 1989; pp. 1–466.
83. Sharma, M. Siberian traps. In *Large Igneous Provinces: Continental, Oceanic and Planetary Flood Volcanism*; Mahoney, J.J., Coffin, M.F., Eds.; American Geophysical Union Geophysical Monograph of New York: New York, NY, USA, 1997; pp. 273–295.
84. Aldanmaz, E.; Pearce, J.A.; Thirlwall, M.F.; Mitchell, J.G. Petrogenetic evolution of late Cenozoic, post-collision volcanism in western Anatolia, Turkey. *J. Volcanol. Geotherm. Res.* **2000**, *102*, 67–95. [[CrossRef](#)]
85. Tao, L.; Zhang, H.; Wu, J.; Zhou, X.; Zhang, L. Magma Generation of Magnetite-Rich Intermediate-Mafic Rocks and Its Mantle Processes in the Southwestern Alxa Block, NW China. *J. Earth Sci.* **2022**, *33*, 161–176. [[CrossRef](#)]
86. Shannon, R.D. Revised effective ionic radii and systematic studies of interatomic distances in halides and chalcogenides. *Acta Crystallogr. Sect. A* **1976**, *32*, 751–767. [[CrossRef](#)]
87. Zhang, Z.; Mahoney, J.J.; Mao, J.; Wang, F. Geochemistry of Picritic and Associated Basalt Flows of the Western Emeishan Flood Basalt Province, China. *J. Pet.* **2006**, *47*, 1997–2019. [[CrossRef](#)]
88. McKenzie, D.; O’Nions, R.K. Partial Melt Distributions from Inversion of Rare Earth Element Concentrations. *J. Pet.* **1991**, *32*, 1021–1091. [[CrossRef](#)]
89. Shaw, D.M. Trace element fractionation during anatexis. *Geochim. Cosmochim. Acta* **1970**, *34*, 237–243. [[CrossRef](#)]
90. Ketin, I. Relations between general tectonic features and the main earthquake regions of Turkey. *Bull. Miner. Res. Expl. Inst. Turk.* **1969**, *71*, 63–74.
91. Walter, M.J. Melting of garnet peridotite and the origin of komatiite and depleted lithosphere. *J. Petrol.* **1998**, *39*, 29–60. [[CrossRef](#)]
92. Liu, S.; Zou, H.; Hu, R.; Zhao, J.; Feng, C. Mesozoic mafic dikes from the Shandong Peninsula, North China Craton: Petrogenesis and tectonic implications. *Geochem. J.* **2006**, *40*, 181–195. [[CrossRef](#)]
93. Hou, G.; Santosh, M.; Qian, X.; Lister, G.S.; Li, J. Configuration of the Late Paleoproterozoic supercontinent Columbia: Insights from radiating mafic dyke swarms. *Gondwana Res.* **2008**, *14*, 395–409. [[CrossRef](#)]
94. Pearce, J.A.; Harris, N.B.W.; Tindle, A.G. Trace Element Discrimination Diagrams for the Tectonic Interpretation of Granitic Rocks. *J. Pet.* **1984**, *25*, 956–983. [[CrossRef](#)]

95. Hawkesworth, C.J.; Turner, S.P.; McDermott, F.; Peate, D.W.; van Calsteren, P. U-Th Isotopes in Arc Magmas: Implications for Element Transfer from the Subducted Crust. *Science* **1997**, *276*, 551–555. [[CrossRef](#)]
96. Pearce, J.A.; Norry, M.J. Petrogenetic implications of Ti, Zr, Y and Nb variations in volcanic rocks. *Contrib. Mineral. Petrol.* **1979**, *69*, 33–47. [[CrossRef](#)]
97. Wood, D.A. The application of a Th–Hf–Ta diagram to problems of tectonomagmatic classification and to establishing the nature of crustal contamination of basaltic lavas of the British Tertiary Volcanic Province. *Earth Planet. Sci. Lett.* **1980**, *50*, 11–30. [[CrossRef](#)]
98. Cabanis, B.; Lecolle, M. Le diagramme La/10-Y/15-Nb/8: Un outil pour la discrimination des séries volcaniques et la mise en évidence des processus de mélange et/ou de décontamination crustale. *Comptes Rendus De L'Académie Des Sci.* **1989**, *309*, 2023–2029.
99. Wu, F.Y.; Wan, B.; Zhao, L.; Xiao, W.J.; Zhu, R.X. Tethyan geodynamics. *Acta Petrol. Sin.* **2020**, *36*, 1627–1674.
100. Zhang, J.; Mattinson, C.G.; Meng, F.; Wan, Y.; Tung, K. Polyphase tectonothermal history recorded in granulitized gneisses from the north Qaidam HP/UHP metamorphic terrane, western China: Evidence from zircon U-Pb geochronology. *GSA Bull.* **2008**, *120*, 732–749. [[CrossRef](#)]
101. Peng, Y. *The Late Hercynian-Indosinian Structural Characteristics of the Zongwulong Belt in North Qaidam Basin*; Chinese Academy of Geological Sciences: Beijing, China, 2015; pp. 1–164. (In Chinese with English abstract)
102. Qin, Y.; Feng, Q.; Chen, G.; Chen, Y.; Zou, K.; Liu, Q.; Jiao, Q.; Zhou, D.; Pan, L.; Gao, J. Devonian post-orogenic extension-related volcano-sedimentary rocks in the northern margin of the Tibetan Plateau, NW China: Implications for the Paleozoic tectonic transition in the North Qaidam Orogen. *J. Asian Earth Sci.* **2018**, *156*, 145–166. [[CrossRef](#)]
103. Sun, Y.G.; Zhang, G.W.; Guo, A.L.; Wang, J. Qinling–Kunlun triple junction and isotope chronological evidence of its tectonic processes. *Geol. China* **2004**, *31*, 372–378. (In Chinese with English abstract)
104. Zhou, C.-A.; Song, S.; Allen, M.B.; Wang, C.; Su, L.; Wang, M. Post-collisional mafic magmatism: Insights into orogenic collapse and mantle modification from North Qaidam collisional belt, NW China. *Lithos* **2021**, *398–399*, 106311. [[CrossRef](#)]
105. Sun, Y.G.; Zhang, G.W.; Wang, J.; Zhan, F.Y.; Zhang, Z.Y. ⁴⁰Ar/³⁹Ar age of the basic sill swarms of two periods in the junction area of Qinling and Kunlun and its tectonic significance. *Acta Geol. Sin.* **2004**, *78*, 65–71. (In Chinese with English abstract)
106. Li, C.S.; Zhang, Z.W.; Li, W.Y.; Wang, Y.L.; Sun, T.; Ripley, E.M. Geochronology, petrology and Hf-S isotope geochemistry of the newly-discovered Xiarihamu magmatic Ni-Cu sulfide deposit in the Qinghai-Tibet plateau, western China. *Lithos* **2015**, *216–217*, 224–240. [[CrossRef](#)]
107. Hu, C.; Li, M.; Feng, C.; Zha, X.; Gao, X.; Meng, J. Petrogenesis and metallogenic potential of the early devonian Yugusayi mafic-ultramafic complex in Qimantagh, East Kunlun orogenic belt. *Int. Geol. Rev.* **2021**, *65*, 1–21. [[CrossRef](#)]
108. Chen, J.; Xie, Z.Y.; Li, B.; Tan, S.X.; Ren, H.; Zhang, Q.M.; Li, Y. Petrogenesis of Devonian Intrusive rocks in Lalingzhuo area, Eastern Kunlun, and its Geological significance. *Mineral. Petrol.* **2013**, *33*, 26–34.
109. Liu, Z.Q.; Pei, X.Z.; Li, R.B.; Li, Z.Z.; Zhang, X.F.; Liu, Z.G.; Guo, J.F. LA-ICP-MS Zircon U-Pb Geochronology of the Two Suites of Ophiolites at the Buqingshan Area of the Anyemaqen Orogenic Belt in the Southern Margin of East Kunlun and its Tectonic implication. *Acta Geol. Sin.* **2011**, *85*, 185–194.
110. Zhao, W.T.; Liu, S.F.; Chen, M. Detrital zircon geochronology and its geological significance from Turgendaban Formation in Shengge area of Zongwulong Belt. *China Min. Mag.* **2020**, *29*, 279–283, (In Chinese of English abstract).

Disclaimer/Publisher's Note: The statements, opinions and data contained in all publications are solely those of the individual author(s) and contributor(s) and not of MDPI and/or the editor(s). MDPI and/or the editor(s) disclaim responsibility for any injury to people or property resulting from any ideas, methods, instructions or products referred to in the content.